JOURNAL OF GEOPHYSICAL RESEARCH: SOLID EARTH, VOL. 118, 4599–4627, doi:10.1002/jgrb.50244, 2013

A three-step maximum a posteriori probability method for InSAR data inversion of coseismic rupture with application to the 14 April 2010 M_w 6.9 Yushu, China, earthquake

Jianbao Sun,[1] Zheng-Kang Shen,[2,3] Roland Bürgmann,[4] Min Wang,[1] Lichun Chen,[5] and Xiwei Xu[5]

Received 17 June 2011; revised 20 March 2013; accepted 7 June 2013; published 27 August 2013.

[1] We develop a three-step maximum a posteriori probability method for coseismic rupture inversion, which aims at maximizing the a posterior probability density function (PDF) of elastic deformation solutions of earthquake rupture. The method originates from the fully Bayesian inversion and mixed linear-nonlinear Bayesian inversion methods and shares the same posterior PDF with them, while overcoming difficulties with convergence when large numbers of low-quality data are used and greatly improving the convergence rate using optimization procedures. A highly efficient global optimization algorithm, adaptive simulated annealing, is used to search for the maximum of a posterior PDF ("mode" in statistics) in the first step. The second step inversion approaches the "true" solution further using the Monte Carlo inversion technique with positivity constraints, with all parameters obtained from the first step as the initial solution. Then slip artifacts are eliminated from slip models in the third step using the same procedure of the second step, with fixed fault geometry parameters. We first design a fault model with 45° dip angle and oblique slip, and produce corresponding synthetic interferometric synthetic aperture radar (InSAR) data sets to validate the reliability and efficiency of the new method. We then apply this method to InSAR data inversion for the coseismic slip distribution of the 14 April 2010 M_w 6.9 Yushu, China earthquake. Our preferred slip model is composed of three segments with most of the slip occurring within 15 km depth and the maximum slip reaches 1.38 m at the surface. The seismic moment released is estimated to be 2.32e+19 Nm, consistent with the seismic estimate of 2.50e+19 Nm.

Citation: Sun, J., Z.-K. Shen, R. Bürgmann, M. Wang, L. Chen, and X. Xu (2013), A three-step maximum a posteriori probability method for InSAR data inversion of coseismic rupture with application to the 14 April 2010 M_w 6.9 Yushu, China, earthquake, *J. Geophys. Res. Solid Earth*, *118*, 4599–4627, doi:10.1002/jgrb.50244.

1. Introduction

[2] Space geodetic techniques, particularly GPS and InSAR, have become vital tools for earthquake and crustal deformation studies in recent years. Data measured using these techniques have been widely used for inversion of coseismic slip and other sources of crustal deformation involving the determination of best fit source parameters. A number of model inversion methods have been developed, so that the data can be effectively used for exploring geophysical sources of crustal deformation. In this study we propose a new coseismic slip inversion method and apply it to study the slip distribution of the 14 April 2010 M_w 6.9 Yushu, China earthquake.

[3] Detailed reviews of the inversion methods, especially those using the Monte Carlo inversion techniques, have been given by *Fukuda and Johnson* [2008, 2010] and *Sambridge and Mosegaard* [2002]. For the ones closely related to this study, *Bürgmann et al.* [2002] used a constrained nonlinear optimization algorithm to estimate the fault geometry of the 1999 Düzce (Turkey) earthquake, assuming a uniform-slip dislocation model. They applied a quasi-Newton algorithm for the nonlinear fault geometry parameter inversion and a positive-constrained least squares algorithm for the slip-distribution inversion, where a common sign of the strike-slip and/or dip-slip component is imposed on the slip solutions [*Árnadóttir and Segall*, 1994]. The quasi-Newton algorithm is a derivative-based method, which requires many restarts from different starting models to guarantee the objective function reaching the global minimum. A similar algorithm is used

Additional supporting information may be found in the online version of this article.

[1]State Key Laboratory of Earthquake Dynamics, Institute of Geology, China Earthquake Administration, Beijing, China.
[2]Department of Earth and Space Sciences, University of California, Los Angeles, California, USA.
[3]Department of Geophysics, Peking University, Beijing, China.
[4]Department of Earth and Planetary Science, University of California, Berkeley, California, USA.
[5]Key Laboratory of Active Tectonic and Volcano, Institute of Geology, China Earthquake Administration, Beijing, China.

Corresponding author: J. Sun, State Key Laboratory of Earthquake Dynamics, Institute of Geology, China Earthquake Administration, Beijing 100029, China. (sunjianbao@gmail.com)

2169-9313/13/10.1002/jgrb.50244

by *Shen et al*. [2009] for the coseismic slip model of the 2008 Wenchuan (China) earthquake, for which they simultaneously inverted for the fault geometry and the slip-distribution model. *Jonsson et al*. [2002] applied a simulated annealing algorithm and a derivative-based method in succession to invert for the 1999 Hector Mine earthquake fault dips (assuming uniform-slip on fault planes) and a positive-constrained least squares algorithm to invert for the variable strike slip independently. The simulated annealing algorithm is a global optimization method, which has the capability to find the global minimum in principle. *Fialko* [2004] used a forward grid search algorithm and a constrained least squares method to invert for the fault dips and slip distribution of the 1992 Landers earthquake in a series of iterations. *Wright et al*. [1999] adopted a hybrid Monte Carlo, downhill simplex inversion technique to search for the best fit model of the 1995 Dinar (Turkey) earthquake with a uniform-slip assumption. They restarted 1000 Monte Carlo inversions to ensure that the final misfit is the global minimum. *Funning et al*. [2005] used the same method to invert for the fault geometry of the 2004 Bam (Iran) earthquake, and a fast positive-constrained least squares solution [*Bro and Jong*, 1997] to invert for the slip distribution of the earthquake with a smoothing constraint. *Yabuki and Matsu'ura* [1992] developed the Bayesian slip inversion formulation and used the Akaike's Bayesian Information Criterion (ABIC) [*Akaike*, 1980] to objectively determine the smoothing factor of slip models. They assume that the fault geometry is already known before the inversion. *Fukahata and Wright* [2008] extended the ABIC method to invert for the fault dip with the smoothing parameter (called "hyperparameters") together. Once the hyperparameters are determined from ABIC, the slip-distribution model is found based on the maximum likelihood method.

[4] However, as *Fukuda and Johnson* [2008] noted, the ABIC methods are incorrect when the positivity constraints are applied, and this led *Fukuda and Johnson* [2008] to develop the fully Bayesian inversion (FBI) method for slip inversion. In this method, they provided a complete probability solution for the problem with or without positivity constraints, which determines an objective smoothing factor, unknown relative weights of multiple data sets, and fault geometry and slip vectors on multiple patches of fault planes in one process. Recently, *Minson* [2010] developed a Bayesian approach called "Cascading Adaptive Tempered Metropolis In Parallel" for earthquake source inversion studies, which is based on transitional Markov chain Monte Carlo and has the advantage of parallel implementation and can be used for inversion of high-dimension geophysical problems.

[5] In summary, when we implement an inversion, the parameters to be determined are as follows: fault geometry, smoothing factor, data weights when multiple data sets are used, and slip vectors of small patches on subdivided fault planes. Additional "nuisance parameters," such as the static offsets or orbit ramps in InSAR data, need to be accounted for in the inversion as well, if they are not determined and removed in data processing stages. In the inversion schemes we summarized above, there are some critical options that may influence the final results: (1) using uniform-slip assumption when inverting for fault geometry or inverting for fault geometry and distributed slip simultaneously; (2) using the positivity constraint on fault slip inversion or not; (3) adopting a global optimization search method or a derivative-based method for nonlinear parameter inversion; (4) choice of an objective regularization parameter, such as the smoothing factor in the fault slip-distribution inversion; and (5) ways to weight multiple data sets so that different observations can be reconciled in one inversion.

[6] *Fukahata and Wright* [2008] and *Sun et al*. [2008] reported that the uniform-slip assumptions can bias the fault geometry inversion and the best fault geometry for a spatially variable slip distribution is not guaranteed under this assumption. The positivity constraint is often a necessary piece of prior information for geodetic inversion because few data sets can constrain a fault slip model unambiguously given the noise level in the data and/or the limitations of the form of observation, such as ambiguities in the interpretation of displacements in the InSAR line of sight (LOS). However, the positivity constraint violates the assumed Gaussian error distribution of slip models in least squares solutions, and the problem can then be solved in a fully Bayesian inversion using a non-Gaussian posterior probability density function (PDF) and Monte Carlo sampling technique [*Fukuda and Johnson*, 2008]. In order to find the global minimum of an objective function for nonlinear equations, global optimization algorithms, such as the simulated annealing algorithm, the genetic algorithm, etc., are widely used for geophysical problems due to their high efficiency and capability of jumping out of local minimum regions of a high-dimensional parameter space [*Sambridge and Mosegaard*, 2002], whereas the derivative-based methods need a lot of restarts to avoid the inversion becoming trapped in a local minimum [*Bürgmann et al*., 2002; *Shen et al*., 2009]. The probability inversion methods, such as the ABIC method and the FBI method, seek to determine an objective smoothing factor, which are superior approaches compared to the traditional method using a trade-off curve between the slip model roughness and misfit values [*Fukuda and Johnson*, 2008]. The relative weights of multiple data sets in an inversion, which are often assigned based on subjective considerations, rather than determined by an objective function, also directly influence the inversion results. The FBI method developed by *Fukuda and Johnson* [2008] and the mixed linear-nonlinear Bayesian inversion (MBI) method developed by *Fukuda and Johnson* [2010] address most of the issues we summarized above and give complete solutions for fault slip inversion in rigorous mathematical forms.

[7] In this study, we follow the FBI method and the MBI method and continue to overcome two inversion difficulties associated with them, with a new method called the three-step maximum a posteriori probability (MAP) inversion, which we argue can deal with the problems better than the FBI method and MBI method. We first describe the inversion difficulties of the FBI and MBI methods in section 2.1 and then present the three-step MAP inversion method for solving these problems. Next, we provide the procedures and algorithms for the three-step MAP inversion method for geodetic data. Third, we apply the method to an inversion using two synthetic InSAR data sets for verification of the reliability and efficiency of the method. Finally, we apply the method to the coseismic slip-distribution inversion of the 14 April 2010 M_w 6.9 Yushu (Qinghai, China) earthquake using InSAR observations, and the solution is compared with the inversion results using the FBI method. We also use a checkerboard model and the corresponding synthetic data sets with

realistically simulated noise, as model resolution tests for the Yushu earthquake inversion.

2. Three-Step MAP Method for Fault Slip Distribution Inversion

2.1. FBI and MBI Methods

[8] The Monte Carlo methods are appropriate for highly nonlinear inverse problems with complex misfit functions and can be classified into the global optimization methods and the ensemble inference methods in geophysical inversion [*Sambridge and Mosegaard*, 2002]. The former approach intends to find one best fit model, which satisfies certain criteria, such as minimization/maximization of a designed objective function with a Monte Carlo sampling approach. In contrast, an ensemble inference method combines the prior information with the likelihood function of a geophysical problem and produces the joint posterior probability density function (PDF). Then the Monte Carlo sampling technique is used to sample the posterior PDF and to infer the geophysical parameters based on the sampled ensemble models. The FBI method for slip-distribution inversion belongs to the ensemble inference category of Monte Carlo methods, whose counterpart for obtaining slip solution is the least squares method, which involves matrix inversion when the fault geometry is known. However, when the fault geometry is unknown, we may need to draw on both of the Monte Carlo and least squares methods. The MBI method involves the combination of the ensemble-inference Monte Carlo method (or Bayesian method) with the least squares method to solve inverse problems.

[9] The FBI method proposed by *Fukuda and Johnson* [2008] describes the slip-distribution inversion problem as a posterior PDF sampling and ensemble inference process. In addition to the fault geometry parameters, the smoothing factor, relative weights of data sets, and slip vectors of fault patches are all solved for simultaneously with the Monte Carlo inversion scheme, without using the least squares inversion. This is actually what the so-called fully Bayesian inversion method means. It is a highly nonlinear inversion method, because every parameter we listed above is included in the posterior PDF and must be sampled in one process. It necessitates the Monte Carlo sampling technique due to the complex form of the target non-Gaussian distribution of posterior PDF of the slip solution and has many advantages over the classical inversion methods as those presented by *Fukuda and Johnson* [2008] and *Minson* [2010].

[10] However, when the positivity constraints on fault slip (or slip bounds) are not needed, the least squares slip inversion method can be combined with the Monte Carlo nonlinear parameter sampling process as is used in the mixed linear-nonlinear Bayesian inversion (MBI) method [*Fukuda and Johnson*, 2010]. The MBI method is more efficient than the FBI method because it has much less number of the parameters to be inverted nonlinearly than the FBI method. The theoretical basis of the MBI method is that the posterior PDF of inverse problems can be separated into two parts, namely the posterior PDF of linear parameters and the posterior PDF of nonlinear parameters [*Fukuda and Johnson*, 2010].

[11] We, however, recognize two major difficulties of these methods in the inversion of InSAR data, which normally have complex noise characteristics, large number of data points and LOS ambiguities, and the complex parameter space structure may complicate the inversion process using the FBI and MBI methods. One difficulty is the huge computation cost and/or slow convergence rate when a large number of parameters are inverted, such as in the case of an earthquake that ruptured multiple fault segments, or when several data sets with high spatial resolution are used. This led *Fukuda and Johnson* [2010] to develop the MBI method. However, both MBI and FBI methods use the Markov chain Monte Carlo (MCMC) technique to sample the parameter space based on the Metropolis rule, and their acceptance probabilities are equivalent to that of the simulated annealing (SA) algorithm with a constant temperature, and hence the methods are much slower on convergence rate than this global optimization method.

[12] Another difficulty lies in the determination of the parameter step sizes for inversion, and this sometimes leads to convergence difficulties in the inversion. A step size that is too large may make the inversion difficult to converge and the proposed models could repeatedly fall in very low probability regions, in which case the Markov chain can remain stuck in a model and its vicinity for many cycles. A step size that is too small can lead to an inefficient inversion or bring the inversion to be trapped in a sub-region and never sample the rest of the parameter space, if the probability distribution is defined over disconnected regions [*Agostini*, 2003]. This problem is not easy to solve as we usually know little about the structure of the parameter space to be explored [*Gelman et al.*, 1995; *Miller et al.*, 2000]. *Fukuda and Johnson* [2008] adopt a trial and error strategy to determine a suitable step size; however, one has to restart the FBI or MBI process many times to test the efficiency of the inversion even if the method allows some degree of randomness on the step size (a maximum jump size is assigned). In our experience, when the observation data set has strong noise, such as InSAR data with random noise due to temporal decorrelation effects and strong spatially correlated atmospheric delay [*Zebker et al.*, 1997], the FBI and MBI methods have difficulty to converge on a reasonable solution within finite time.

2.2. Introduction of the Three-Step MAP Inversion Method

[13] We propose to use an inversion method closely related to the FBI and MBI methods, the three-step MAP inversion method to overcome the two difficulties mentioned in the previous section. This approach belongs to the optimization class of Monte Carlo methods, rather than the ensemble inference methods as in the FBI and MBI methods. A simple flowchart about the method is provided in Figure 1. In the first step, we use an advanced global optimization algorithm, adaptive simulated annealing (ASA) [*Ingber*, 1993], to maximize the posterior PDF (its logarithm is used to avoid numerical overflow) of fault slip solution and simultaneously invert for the fault geometry parameters, smoothing factor, relative data weights, and slip distribution. We adopt the posterior PDF formulation of the MBI method presented by *Fukuda and Johnson* [2010] as the objective function for the optimization. In the ASA inversion, the least squares method is adopted for slip inversion without positivity constraints applied, as in the MBI method. For InSAR data inversion, we also need to invert for a first- or second-order orbital ramp due to inaccurate orbit models of radar satellites,

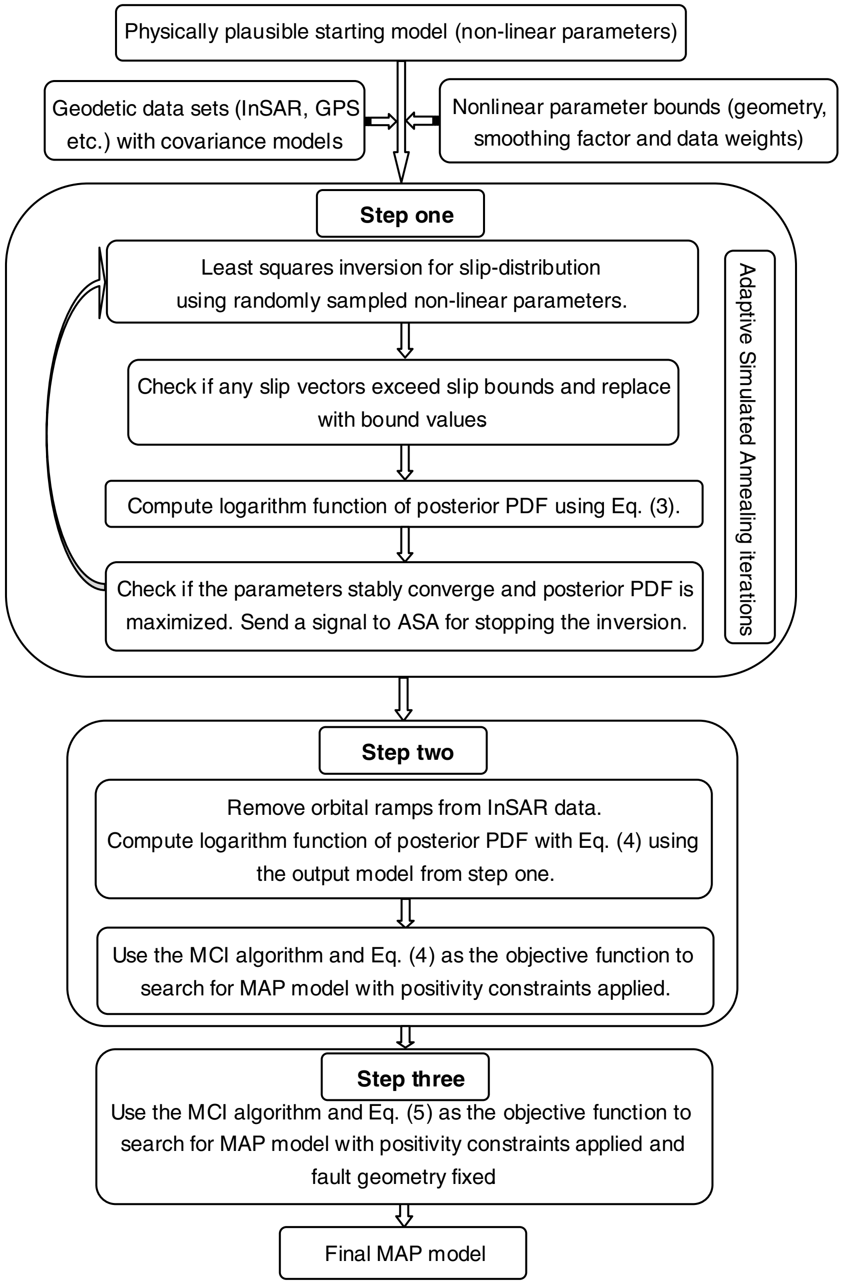

Figure 1. The flowchart of the three-step MAP inversion. The three steps are sequentially implemented, with the output model of the prior step as the initial model of the successive step. The logarithm functions of the objective functions are used to avoid numerical overflow. The three steps are connected by the optimized models of every step, rather than the objective functions and their values.

if it cannot be completely removed in the data processing stage. By using the standard least squares method for slip inversion with nonlinear parameter sampling in ASA optimization, the inversion efficiency is greatly improved. It is possible that some slip vectors exceed the valid ranges/bounds for earthquake rupture, such as slip reversals. In some extreme cases, the smoothing factor may become exceptionally small for a very rough slip solution without slip constraint (smaller smoothing factor means weak smoothing constraint in our study), while the posterior PDF is at its real maximum in full parameter space. In order to overcome this problem, we replace the slip vectors that fall outside of the specified ranges with slip bound values in every ASA iteration. The slip bounds, assigned before the inversion, are compatible with the physics and tectonic style of a particular earthquake rupture. For simplicity, we call the operation “slip-replacement” and refer to the fault slip ranges or bounds as “positivity constraints” hereafter. Then the posterior PDF is calculated and optimized in the ASA inversion. In the next ASA iteration, the standard least squares is still used without positivity constraints applied for satisfying the requirement of the objective function. Through applying this trick, the inversion converges quickly to a physically plausible solution, and it can be compared with other data source inversions, such as a seismic waveform inversion. In the first step, the ASA inversion brings us to a model very close to the "true" solution and guarantees the global optimization of the model parameters.

[14] In the second step, we implement an independent inversion and use the optimized model from step one as the initial model. The orbit ramp inverted from step one is removed from the observation data and the data covariance is also updated if necessary, such as when a full covariance model is used. We deem that the optimized solution from step one has jumped over all of the local maximum regions in parameter space due to the global optimization algorithm adopted and continue to optimize posterior PDF using a Monte Carlo inversion (MCI) technique, subject to positivity constraints similar to the FBI method. The MCI algorithm is used for uniform random parameter space searching with a specified step size. The linear and nonlinear parameters all have their bounds as prior constraints in the MCI sampling. We do not apply a standard global optimization method in the second or the third step of the MAP inversion because the starting model is already an optimized one after the first step of the MAP inversion. The posterior PDF with positivity constraint of the FBI method [*Fukuda and Johnson*, 2008] is adopted as the objective function in the optimization in the second step, and we use a similar sampling procedure as that implemented in the FBI method for the inversion. The fault geometry parameters are included in the posterior PDF in this step of the MAP inversion. The final posterior PDF from the first step is transformed into the posterior PDF of the second step, so that the objective functions of the two steps can be compared with the same criterion. The parameters to be inverted include the slip vectors on the subdivided fault patches in addition to the nonlinear parameters inverted in step one. In other words, we sample every slip vector in assigned slip ranges or bounds in the optimization, rather than invert for slip distribution with least squares solution as in step one. The latter is equivalent to sampling the slip vectors of the whole fault plane once in one step of the ASA inversion, while the former samples the slip vectors N times, where N equals to the number of subdivided fault patches.

[15] In the third step, we fix the fault geometry acquired from step one and step two sequentially, and simultaneously invert for the slip distribution with positivity constraints applied and other parameters. The similar posterior PDF formulation as that in step two is adopted as the objective function in the optimization, and we use the same sampling method implemented in step two for the inversion. Through this step of the MAP inversion, we reduce the slip artifacts introduced by the potential trade-off effects between the slip and fault geometry parameters and improve the slip-distribution model further. In all of the steps, the first step of the MAP inversion is essential for coseismic data inversion because it is a highly efficient global optimization procedure and guarantees the inversion approaching the global maximum, while the other two steps can be omitted in the three-step MAP inversion if the first step inversion already provided a satisfactory model and if they improve the results little.

[16] By using the three-step MAP inversion scheme, we can overcome the two difficulties in the FBI and MBI method. The step size problem will not prevent the convergence of the inversion because we only intend to find the maximum posterior PDF in every step of inversion, and the proposed models cannot repeatedly fall in low probability regions. In addition, the step size is determined automatically by the ASA algorithm [*Ingber*, 1993] in the first step, which guarantees the global optimization of the posterior PDF in the inversion. The efficiency of the first step of the MAP inversion is much higher than that of the MBI method due to the highly efficient simulated annealing algorithm adopted in the global optimization, rather than the MCMC sampling method used in the Bayesian inversion algorithm. The other two steps use the MCI sampling algorithm and the output of the ASA inversion as a starting point. Hence, the convergence rate of these two steps is also faster than that of the FBI method because the efficiency of the Monte Carlo inversion depends on the distance between the initial model guess and the final solution. However, if the initial model from the first step of the MAP inversion is not applied, the global optimization in the second step would not be guaranteed due to the limitation of the simple MCI algorithm used here. The method can be used for any kind of data sets irrespective of the noise level, and the solution would not be trapped in low probability regions, as long as the data sets are self-consistent and not contrary to each other. However, because the MAP inversion is a point estimate process, the advantage of the Bayesian method for estimating slip model uncertainties is meaningless in the three-step MAP method. We then prefer to use the traditional checkerboard model method for this purpose, so that the uncertainties of the fault geometry and fault slip-distribution models can be qualitatively and quantitatively analyzed.

2.3. Three-Step MAP Inversion Algorithms

[17] We have summarized the main procedures of the three-step MAP inversion and their usefulness in fault slip inversions in section 2.2 and illustrate the method with a flowchart in Figure 1. In this section, we provide the main mathematical formulations of this method. Since it is based on the adaptive simulated annealing algorithm [*Ingber*, 1993], the fully Bayesian inversion algorithm [*Fukuda and Johnson*, 2008] and the mixed line-nonlinear Bayesian inversion algorithm [*Fukuda and Johnson*, 2008], we refer the readers to the corresponding papers for details on the algorithm implementation.

[18] For geodetic observation and its inverse problem, following the formulation of *Fukuda and Johnson* [2008], the nonlinear system composed of the fault geometry parameters and corresponding slip distribution can be written as

$$d = G(m)s + \varepsilon \tag{1}$$

where m contains the fault geometry parameter, s is the fault slip vector on every boundary element, G is the Green's function matrix in elastic dislocation theory, such as in a half-space model [*Okada*, 1992] or a layered Earth model [*Wang et al.*, 2003], ε is the data error array of the observation system following a Gaussian distribution, and d is the column vector of deformation observations from GPS and InSAR.

[19] In the first step of the MAP inversion, we adopt a widely used simulated annealing algorithm for global optimization, the ASA algorithm developed by *Ingber* [1993], which has more than 100 options for algorithm adjustments

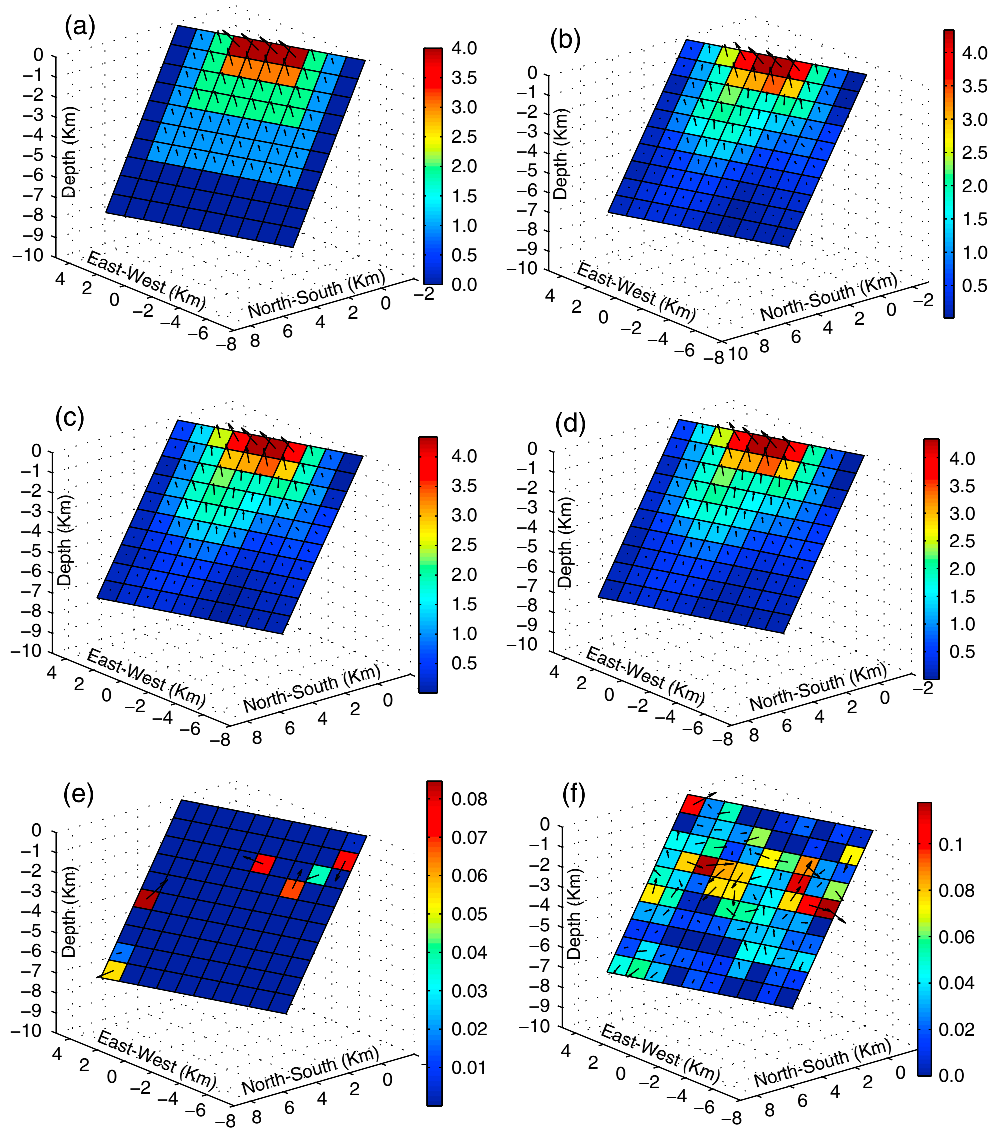

Figure 2. Verification of the three-step MAP inversion method with synthetic InSAR data sets. (a) A designed 45° dipping fault model with oblique slip on a 10 km by 10 km fault plane. (b–d) The models from the first, second, and third steps of the MAP inversion, respectively. (e) The difference between the models from the first and second steps of the MAP inversion. (f) The difference between the models from the first and third steps of the MAP inversion. All of the slip vectors are in unit of meters.

for particular problems, is more efficient than the conventional simulated annealing algorithms, and is robust in solving highly nonlinear optimization problems. We use the ASA algorithm as a driver to search for the maximum of the posterior PDF of the slip solutions. The most effective way to do the global optimization in the first step of the MAP inversion is to use the posterior PDF of the MBI method as the objective function, where the linear and nonlinear inversions are combined in a Bayesian inversion [*Fukuda and Johnson*, 2010]. We do not use the posterior PDF of the FBI method with positivity constraint here because the parameter number would be too large to be effectively inverted in the global optimization method. In addition, the orbital ramp of InSAR data is also difficult to be effectively inverted with the posterior PDF of the FBI method.

[20] The simulated annealing (SA) algorithm, such as the ASA algorithm used here, is a highly efficient global optimization method, which is widely used in geophysical inversion [*Sen and Stoffa*, 1995]. The general form of the acceptance probability of the SA algorithm is $P_{\mathrm{accept}} = \min\left(1, \exp\left(-\frac{p\left(x^{(t)}\right)-p(x')}{T}\right)\right)$ with the temperature variable T controlling the convergence rate, $p(x')$ and $p(x^{(t)})$ are the candidate state's (x') and current state's ($x^{(t)}$) posterior PDF (in logarithm function). Note that we intend to maximize the posterior PDF, rather than minimize an energy function as the standard SA algorithm. With the temperature $T \to 0$, the algorithm reduces to the greedy algorithm of the classical Monte Carlo Inversion (MCI) [*Sen and Stoffa*, 1995]. With the temperature being a constant $T = 1$, the algorithm is similar

Table 1. Parameters From Synthetic InSAR Data Inversion Using the Three-Step MAP Method

	Dip (deg)	Strike (deg)	Location X (km)	Location Y (km)	Weight 1	Weight 2	Smoothing Factor	Max posterior PDF (Logarithm)	WRSS
Designed model	45.0	248.6	0.0	0.0					
Parameter bounds	10 ~ 90	198 ~ 298	−15 ~ 15	−15 ~ 15	0.1 ~ 20	0.1 ~ 20	0.1 ~ 50		
Step 1	40.0	249.6	−0.02	−0.12	0.98	1.01	0.99	−1365.8	2686.6
Step 2	40.2	249.7	−0.03	−0.12	0.97	0.99	1.74	−1315.9	2731.2
Step 3	40.2	249.7	−0.03	−0.12	0.97	1.00	1.82	−1309.7	2731.2

to the Metropolis rule used in the FBI method with $P_{\text{accept}} = \min\left(1, \frac{p(x')}{p(x^{(t)})}\right)$. The ASA algorithm over a D dimensional space has an annealing schedule for temperature T decreasing exponentially in annealing time k, $T = T_0 \exp\left(-ck^{1/D}\right)$, where T_0 is the initial temperature at the start of the inversion and c is a control parameter for specific problems. The ASA algorithm also has an option called "re-annealing," which allows the adaptive changing of the parameter sensitivities in the multidimensional parameter space and hence increases the inversion efficiency adaptively.

and then use the least squares method to invert equation (2) to get the fault slip solution s. However, in the MBI method, the Monte Carlo technique is used to sample the posterior PDF of the slip solution to equation (2), which is separated into two parts when the positivity constraint is not applied, namely the posterior PDF of nonlinear parameters and the posterior PDF of linear parameters. Then the MCMC method is used to sample the posterior PDF of nonlinear parameters and the standard least squares method is used to invert for slip distribution. The posterior PDF of nonlinear parameters can be written as equation (3) rearranged following [*Fukuda and Johnson*, 2010]:

$$p(m, \sigma_1, \sigma_2, \ldots, \sigma_k, \alpha^2 | d_1, d_2, \ldots, d_k) = \begin{cases} \frac{1}{Z}\left[\prod_{k=1}^{K}\left(\sigma_k{}^2\right)^{-N_k/2}\right]\left(\alpha^2\right)^{-M/2}\left|A^TA\right|^{-1/2}\exp\left[-\frac{1}{2}f(s^*)\right], & \text{for } \sigma > 0, \alpha > 0, \\ 0, & \text{otherwise} \end{cases} \tag{3}$$

$$f(s) = (y - As)^T(y - As)$$

[21] A general equation for geodetic data inversion, considering the regularization (smoothing) of slip solution, relative weights of multiple data sets and fault geometry parameters, can be written as

$$\begin{pmatrix} R^{-1/2}d \\ 0 \end{pmatrix} = \begin{pmatrix} R^{-1/2}G(m) \\ \alpha^{-1}L \end{pmatrix} s = As, A = \begin{pmatrix} R^{-1/2}G(m) \\ \alpha^{-1}L \end{pmatrix}, y = \begin{pmatrix} R^{-1/2}d \\ 0 \end{pmatrix} \tag{2}$$

where R is a diagonal matrix with its diagonal terms being $\sigma_1^2 \sum_1, \sigma_2^2\sum_2, \cdots, \sigma_K^2\sum_K$, K is the total number of data sets, $\sigma_1, \sigma_2, \ldots, \sigma_k$ are the relative weights of individual data set, $\sum_1, \sum_2, \ldots, \sum_K$ are the covariance matrixes of individual data set, d is observation data composed of K data sets $\left[d_1^T, d_2^T, \ldots, d_K^T\right]^T$, m and s are the same as in equation (1), $G(m)$ is the Green's function composed of $[G_1(m)^T, G_2(m)^T, \ldots, G_K(m)^T]^T$, α is the smoothing factor of the slip-distribution solution (note that the reciprocal of α^{-1} is used in our implementation, and a larger α means stronger smoothing), L is the finite difference approximation of the Laplacian operator used for the slip-distribution regularization, A is used as the coefficient matrix of s, and y is a matrix representing the left side of the equation. For simplicity, we consider only one prior $\alpha^{-1}L$ for slip inversion here.

[22] As the smoothing factor, relative data weights and fault geometry parameters (nonlinear parameters) are all unknowns, direct inversion of equation (2) is impossible. The traditional method is to estimate these parameters separately in advance,

where Z is a normalizing constant, M is the dimension of the slip solution, k is the data set number, N_k is the number of data in the kth data set d_k, s^* is the least squares solution to equation (2) when positivity constraint is not applied. The other parameters are the same as in equations (1) and (2). Note that we ignore a term $\left|L^TL\right|^{1/2}$ because it is constant if we do not change the fault decomposition scheme to get fault patches in the inversion. We also assume the prior PDF of nonlinear parameters is constant in their valid ranges.

[23] Both the MBI method and FBI method adopt MCMC method for posterior PDF sampling based on the Metropolis rule, so that the collected models can be used for parameter inference. However, the first step of the MAP inversion implements a global optimization using the posterior PDF (equation (3)) as the objective function. By using a powerful simulated annealing algorithm on the posterior PDF of the MBI method, the optimization problem can be easily solved with high-speed computation. Therefore, fast convergence of the inversion can be obtained, and the two major difficulties of the FBI method are overcome in the first step of the MAP inversion. However, direct optimization of equation (3) by a global optimization algorithm actually obtains a maximum in full parameter space of slip vectors, which is not necessarily rational for geophysical problems because the parameters must be in some ranges/bounds compatible with earthquake physics. Thus, we apply a slip-replacement operation, using the net-slip

and rake bounds as slip constraints, after the standard least squares inversion for slip in every cycle of model generation. This process is repeated in the ASA optimization until convergence (Figure 1). The other inverted parameters are also guided to their valid ranges automatically in this process. Through this simple correction on slip vectors, the first step of the MAP inversion will be able to find a rational solution, while the maximum of equation (3) is found without slip vectors exceeding their valid bounds. The slip bounds can be drawn from other data source inversion, such as the seismic inversion, or from our knowledge on tectonic settings of earthquakes. The influences of the slip-replacement can be verified by evaluating the seismic moment changes within every iteration of the inversion process. This is discussed in section 4.1.

[24] In the second and third steps, we continue to optimize the posterior PDF using the simple MCI algorithm. The posterior PDF of the FBI method is adopted as the objective function in the following two steps because we apply the positivity constraints and do not apply the least squares slip inversion here. By incorporating a likelihood function which relates multiple observations with a model prediction, with a prior probability distribution of the regularization parameter, such as the smoothness of the slip distribution, the joint posterior PDF of a geodetic inversion solution with unknown fault geometry can be written as equation (4) [*Fukuda and Johnson*, 2008]

$$p(m,s,\sigma_1,\sigma_2,\ldots,\sigma_k,\alpha^2|d_1,d_2,\ldots,d_k) = \begin{cases} \dfrac{1}{Z}\left[\prod_{k=1}^{K}\left(\sigma_k{}^2\right)^{-N_k/2}\right]\left(\alpha^2\right)^{-M/2}\exp\left[-\dfrac{1}{2}f\left(m,s,\sigma_1,\sigma_2,\ldots,\sigma_k,\alpha^2\right)\right], & \text{for } s\geq 0,\ \sigma>0,\ \alpha>0, \\ 0, \text{ otherwise} & \end{cases}$$
$$f(m,s,\sigma_1,\sigma_2,\ldots,\sigma_k,\alpha^2) = \sum_{k=1}^{K}\frac{1}{\sigma_k{}^2}\left(d_k - G_k(m)s\right)^T{\sum}_k{}^{-1}\left(d_k - G_k(m)s\right) + \frac{1}{\alpha^2}(Ls)^T(Ls) \tag{4}$$

where $\sum_k$ is the covariance matrix of the kth data set and $G_k(m)$ is the corresponding Green's function. The other parameters are the same as in equation (3). Because $m,\sigma_1,\sigma_2,\ldots,\sigma_k$ and α are unknowns and equation (4) represents a non-Gaussian distribution, the posterior PDF cannot be estimated with the least squares method. In *Fukuda and Johnson* [2008], it is estimated with a MCMC sampling method by using the uniform distributions for unknown parameters to generate the candidate samples and using the Metropolis rule to accept/reject the samples. However, in the second step of the MAP inversion, only the maximum of the posterior PDF in equation (4) is searched for in the vicinity of the "true" solution by using the MCI algorithm.

[25] If the fault geometry is known, equation (4) can be simplified as equation (5) [*Fukuda and Johnson*, 2008]

$$p(s,\sigma_1,\sigma_2,\ldots,\sigma_k,\alpha^2|d_1,d_2,\ldots,d_k) = \begin{cases} \dfrac{1}{Z}\left[\prod_{k=1}^{K}\left(\sigma_k{}^2\right)^{-N_k/2}\right]\left(\alpha^2\right)^{-M/2}\exp\left[-\dfrac{1}{2}f\left(s,\sigma_1,\sigma_2,\ldots,\sigma_k,\alpha^2\right)\right], & \text{for } s\geq 0,\ \sigma>0,\ \alpha>0, \\ 0, \text{ otherwise} & \end{cases}$$
$$f\left(s,\sigma_1,\sigma_2,\ldots,\sigma_k,\alpha^2\right) = \sum_{k=1}^{K}\frac{1}{\sigma_k{}^2}\left(d_k - G_k s\right)^T{\sum}_k{}^{-1}\left(d_k - G_k s\right) + \frac{1}{\alpha^2}(Ls)^T(Ls) \tag{5}$$

[26] The parameters in equation (5) are the same as in equation (4). In the third step of the MAP inversion, equation (5) is adopted as the objective function for optimization using the same sampling method as in step two.

[27] We only provide two equations with positivity constraint here because we always apply this constraint in the three-step MAP inversion. The FBI method spends the computation cost mostly on the Green's function generation and parameter sampling processes, especially when the positivity constraint is applied, because the slip vector on each patch of the fault planes must be sampled to acquire its probability distribution and uncertainty. This process is time consuming when the fault plane includes hundreds of small patches and the observations have thousands of measurement points. This is often the case today when GPS and InSAR data are readily available after an earthquake. In principle, it is the same situation when the second and third steps of MAP inversions are implemented because the only difference between these two steps of the MAP inversions and the FBI lies in their different acceptance probabilities. However, the second and third steps of the MAP inversions start with an already globally

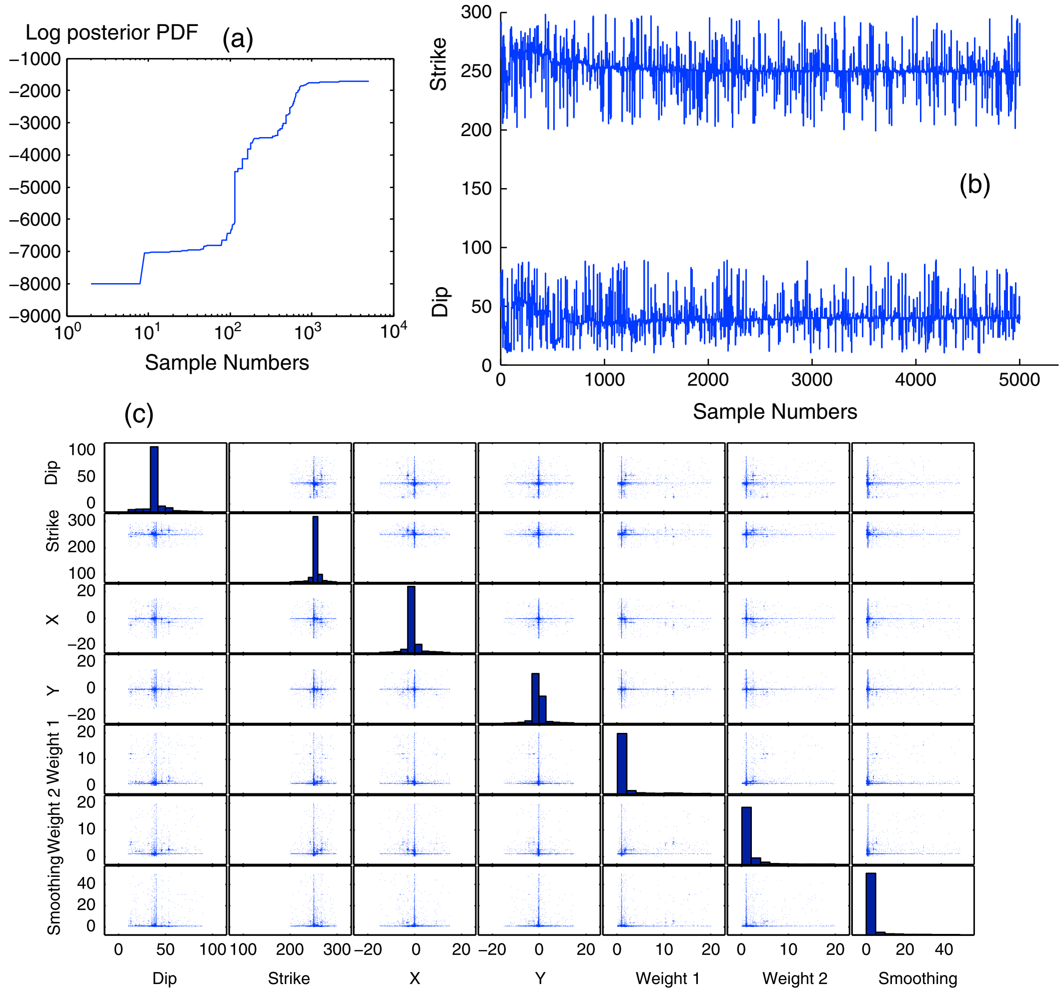

Figure 3. The evolving parameters from the three-step MAP inversion. (a, b) The evolving posterior PDF (in logarithm) and strike/dip angle of the first step of the MAP inversion. (c) The scatterplots of the nonlinear parameter pairs from the first step of the MAP inversion. (d–k) The evolving posterior PDF (in logarithm) and values of the seven parameters of the second (0–1000 samples) and third steps (1000–2000 samples) of the MAP inversion. (l, m) The perturbed noise in the predicted InSAR data in ascending and descending pass LOS geometry. (n, o) The residuals in ascending and descending pass LOS geometry from the three-step MAP inversion. The strike and dip are in unit of degrees. The location "X" and "Y" are in unit of kilometers. The surface deformation of (l-o) are in unit of meters. Others are dimensionless quantities.

optimized model from the first step of the MAP inversion. Therefore, it is generally easy to find a convergent model in these last two inversion steps. Note that we adopt posterior PDF formulations as in equations (3)–(5) for optimization in the three-step MAP inversion, while a simple misfit function measuring differences between observations and model predictions is always used in other Monte Carlo optimization algorithms.

[28] In the following parts, section 2.4, we apply the new three-step MAP inversion method to a designed model with synthetic InSAR data sets for verification, and in section 3.3 we present the inversion of the 14 April 2010 M_w 6.9 Yushu, China earthquake as a real case study. A checkerboard models is used in section 3.3.3 for the resolution test of the Yushu earthquake inversion.

2.4. Verification With Synthetic InSAR Data Sets

[29] In order to illuminate the reliability and efficiency of the three-step MAP method, we design a simple 45° dipping fault model with oblique slip on a 10 km by 10 km fault plane for verification (Figure 2). The fault parameters to be inverted are the dip, strike, and middle point coordinates of the upper edge of the fault plane (Table 1). The fault depth is forced to be zero so that the fault plane reaches the ground surface. The fault plane is subdivided into 10 by 10 patches with a rake angle and a net slip on every patch. We simulated two InSAR data sets in ascending and descending pass LOS geometry, respectively. The spatially correlated noise is propagated into the simulated InSAR data using a simple exponential function, with the maximum variance of 1.0e−4 m^2 and spatially correlated distance of 10 km (Figure 3) [*Funning et al.*, 2005]. This will introduce two weight parameters in the inversion. Another important parameter to be determined in the inversion is the smoothing factor applied to the slip solution, which is addressed by *Fukuda and Johnson* [2010], and is a key factor in this study as well. In order to more directly validate the suitability of the inverted smoothing factor, we deliberately assign

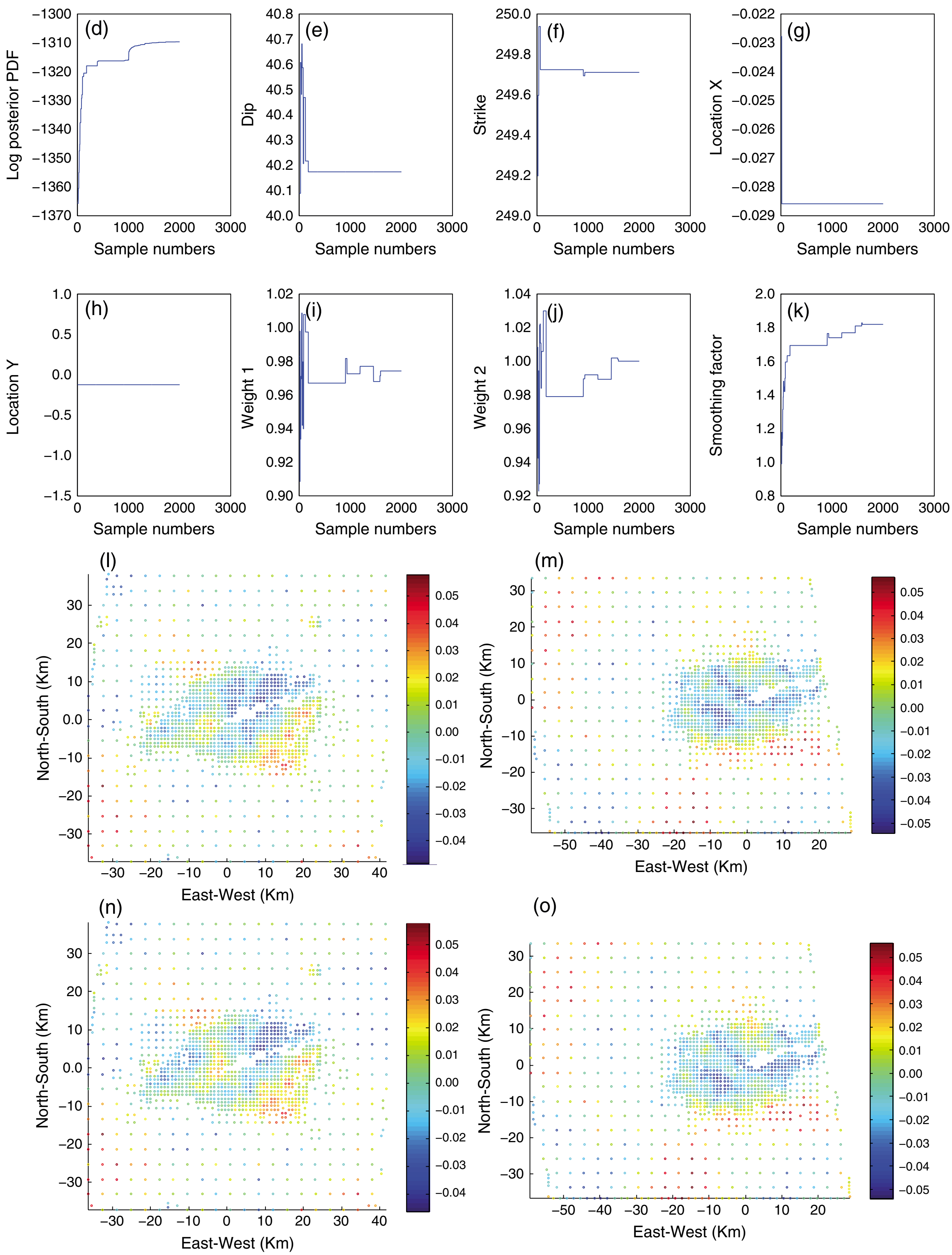

Figure 3. (continued)

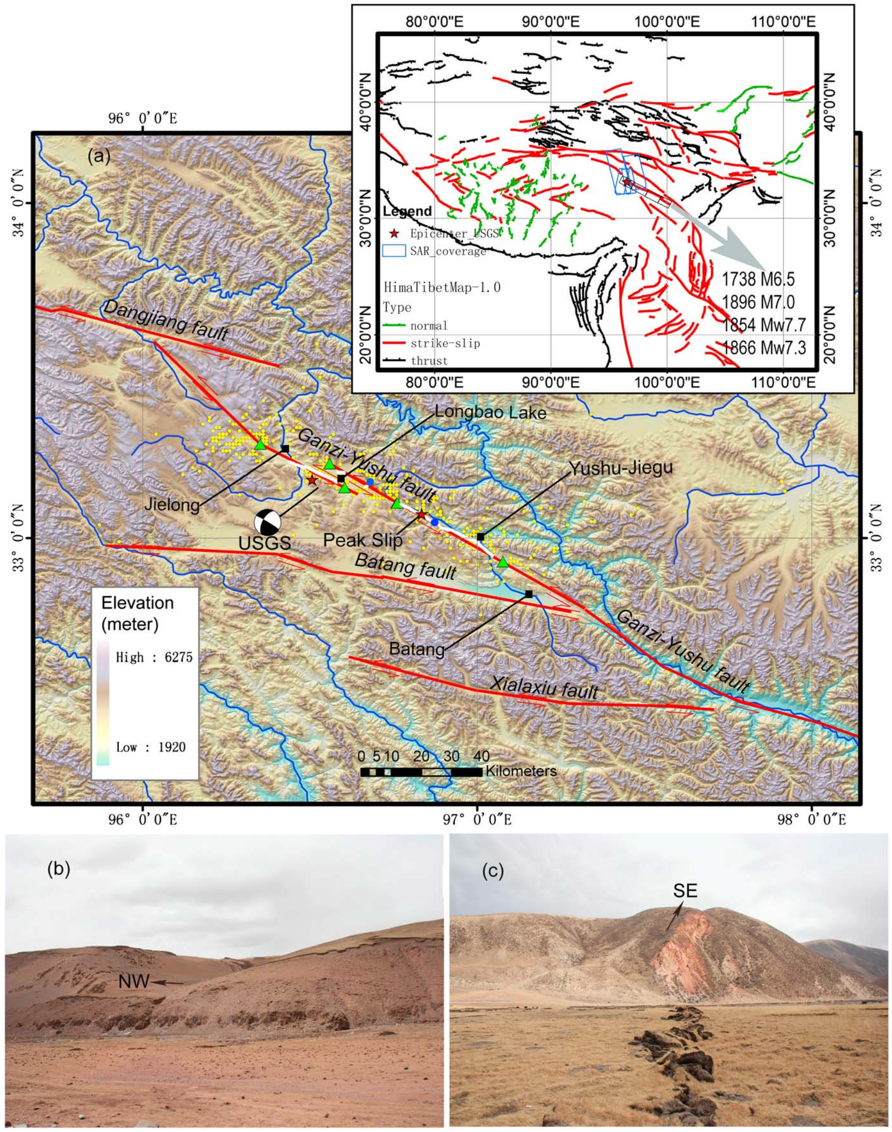

Figure 4. Tectonic map of the Yushu earthquake area. (a) The red lines are the major faults near the fault rupture. The two stars indicate the epicenter from USGS (left) and the maximum surface displacement location (right). The small yellow dots are the aftershocks until 17 May 2010 from the China Digital Seismic Network. The green triangles mark the fault segment endpoints used for modeling in this study. The white lines are the surface ruptures or fissures from the field work of *Chen et al*. [2010] and *Sun et al*. [2010]. The blue lines are rivers of this area. The two blue points on the fault are the photo locations of Figures 4b and 4c. The background is the SRTM DEM [*Farr et al*., 2007]. The inset map shows the earthquake location and the faults from *Taylor and Yin* [2009]. The blue polygons show the SAR data ground coverage of this study. (b and c) Fault scarp photos from field investigation at the west and east blue points, respectively, in Figure 4a. The four black rectangles in the inset map denote the approximated rupture locations of four large historic earthquakes along the Ganzi-Yushu fault.

different rake angles to the four patches on the top row of the fault plane (25° larger than the others of 125°), so that the slip distribution includes a rake rotation near the surface.

[30] The three-step MAP method is applied on the predicted InSAR data, and we monitor every step of the inversion and compare its output with the designed model. In the three-step MAP inversion, the parameter bounds of the net-slip magnitudes and rake angles are set to be 0.0 ~ 10.0 m and 90° ~ 180°, respectively, so that the maximum net slip of 4.0 m and the rake angles of 125° ~ 150° are well defined within the assigned ranges.

[31] The designed model is nearly east-west trending, so that the ground deformation is well captured by both ascending and descending pass InSAR acquisitions in LOS directions. The fault slip increases gradually from 6 km depth to the surface and the maximum slip of 4.0 m occurs at the surface, hence represents a typical surface-ruptured event with complex slip (Figure 2). In the first step, we generated 5001

Table 2. InSAR Data With Precise Orbit Information Processed in This Study

Data Source and Mode	Master Image Date	Slave Image Date	Path or Track[a]	Frame Number	Perpendicular Baseline (m)	Data Quality (Figure No.)
PALSAR FBS	15 Jan 2010	17 Apr 2010	487A[a]	640 ~ 660	~682.6	High coherence (Figure 5b)
PALSAR FBS	28 Nov 2008	18 Apr 2010	138D[a]	2940 ~ 2960	~3410.9	Low coherence (Figure S3)
PALSAR WS	18 Dec 2009	5 May 2010	139D[a]	2950	~1193.0	No interferogram produced
PALSAR WS	4 May 2008	10 May 2010	142D[a]	2950	~788.0	No interferogram produced
Envisat ASAR IS2	15 Feb 2010	26 Apr 2010	498A[a]	32.0°N–34.5° N[b]	~12.5	High coherence (Figure 5a)
Envisat ASAR IS2	8 Jan 2010	23 Apr 2010	455A[a]	32.5°N–35.5° N[b]	~571.8	Low coherence (Figure S2)
Envisat ASAR IS2	3 Nov 2009	1 Jun 2010	004D[a]	32.0°N–34.5° N[b]	~165.0	Moderate coherence (Figure 5e)
Envisat ASAR IS2	3 Nov 2009	27 Apr 2010	004D[a]			Data problem

[a]The letters "A" and "D" represent ascending pass and descending pass, respectively.
[b]The data are cut according to its latitude coverage.

models in the defined parameter space (Table 1), among which 220 models are accepted by the ASA inversion. The maximum of the posterior PDF increased dramatically from -8000.0 to a stable value of -1719.1 according to equation (3) and it was then transformed into a posterior PDF of -1365.8 using equation (4), so that it can be compared in the following steps with the same criterion. It is obvious that after the first step of the MAP inversion, the globally optimized model is already very similar to the designed model (Figure 2b), even along the four surface patches with different rake angles. The fault location and the fault strike have insignificant differences with the designed model (Table 1), and the inverted fault dip is 5° shallower. This is because (1) the perturbed noise in the data prevented the inversion from converging to its true value and (2) the LOS InSAR data sets cannot resolve the 45° dip angle unambiguously in this case. We tried an inversion without noise perturbation in the synthetic data sets, and the dip angle is improved ~3° toward its true value. In the following two steps, the model is refined further (Figures 2c and 2d) with increased posterior PDF. The fault geometry is not improved significantly in the second step, and only few slip vectors are adjusted (Figure 2e). This may indicate that the fault geometry is already well optimized in the first step of the MAP inversion. When the fault geometry is fixed in step three, most of the slip vectors on the fault patches are refined with different magnitudes and rake angles, and the maximum adjustment on the slip is >0.1 m (Figure 2f). Even though the slip improvements are not obvious in the model relative to its maximum (Figure 2d), the overall slips benefit from the improvements when a more precise model is needed, especially for small shallow earthquakes. We take the result of the third step of the MAP inversion as our final optimized model.

[32] In Figure 3, the details about the inversion are provided for illumination of the reliability and efficiency of the process. In the global optimization method using ASA algorithm, the posterior PDF, or the objective function, increased rapidly in the first 1000 models and increased slowly to a stable value in the following 4000 models. It is interesting to see that there are many steep steps in the posterior PDF curve (Figure 3a). This clearly indicates the complexity of the defined parameter space (Table 1) and also shows the high efficiency of the global optimization process. If the two ends of the steep steps represent some disconnected regions in parameter space, then it will be difficult for a FBI/MBI process to converge. The dip angle and fault strike evolve to stable values in the defined ranges, while every possible value is tested in the whole optimization process even if the inversion becomes stably convergent (Figure 3b and S1 in the supporting information). In order to check the trade-off effects between pairs of nonlinear parameters from step one, we plot the parameter pair matrix, including four geometry parameters, two data weights, and a smoothing factor (Figure 3c). The matrix shows well-determined big "cross points" between parameter pairs. This indicates that there are no strong trade-off effects between parameters and every parameter is well determined in the inversion. There are also some other "cross points," but they are obviously smaller than the big ones. This indicates that the parameter space may have multiple peaks and the global optimization is important for the inversion to jump over local maximum regions. Figures 3d–3k show the convergence curves of the second (0–1000 samples) and third steps of the MAP inversion (1000–2000 samples). The changes of the nonlinear parameters in the second step inversion are relatively small, and there are two big jumps at the starts of the second and third steps of MAP inversions in the logarithm posterior PDF curve (Figure 3d). This indicates the necessity for using these two steps to refine the model acquired from step one, even though the nonlinear parameters are well determined from the global optimization step. The perturbed noise in the predicted InSAR data is shown in Figures 3l and 3m, and the residuals of the third step of the MAP inversion are shown in Figures 3n and 3o for comparisons. It is clear that the noise distribution is quite similar to the MAP inversion residuals, though there is a 5° difference on the dip angle between the designed model and the final optimized model. The dip angle difference does not indicate an inversion problem of the three-step MAP inversion.

3. Application of the Three-Step MAP Inversion Method to the 14 April 2010 M_w 6.9 Yushu Earthquake

3.1. Tectonic Background of the 14 April 2010 M_w 6.9 Yushu Earthquake

[33] At 7:49 A.M. Beijing time on 14 April 2010, a devastating earthquake struck the Yushu county of Qinghai province, China, within the interior of the eastern Tibetan Plateau. The event is the largest to strike China since the 2008 Wenchuan earthquake located ~700 km away. The death

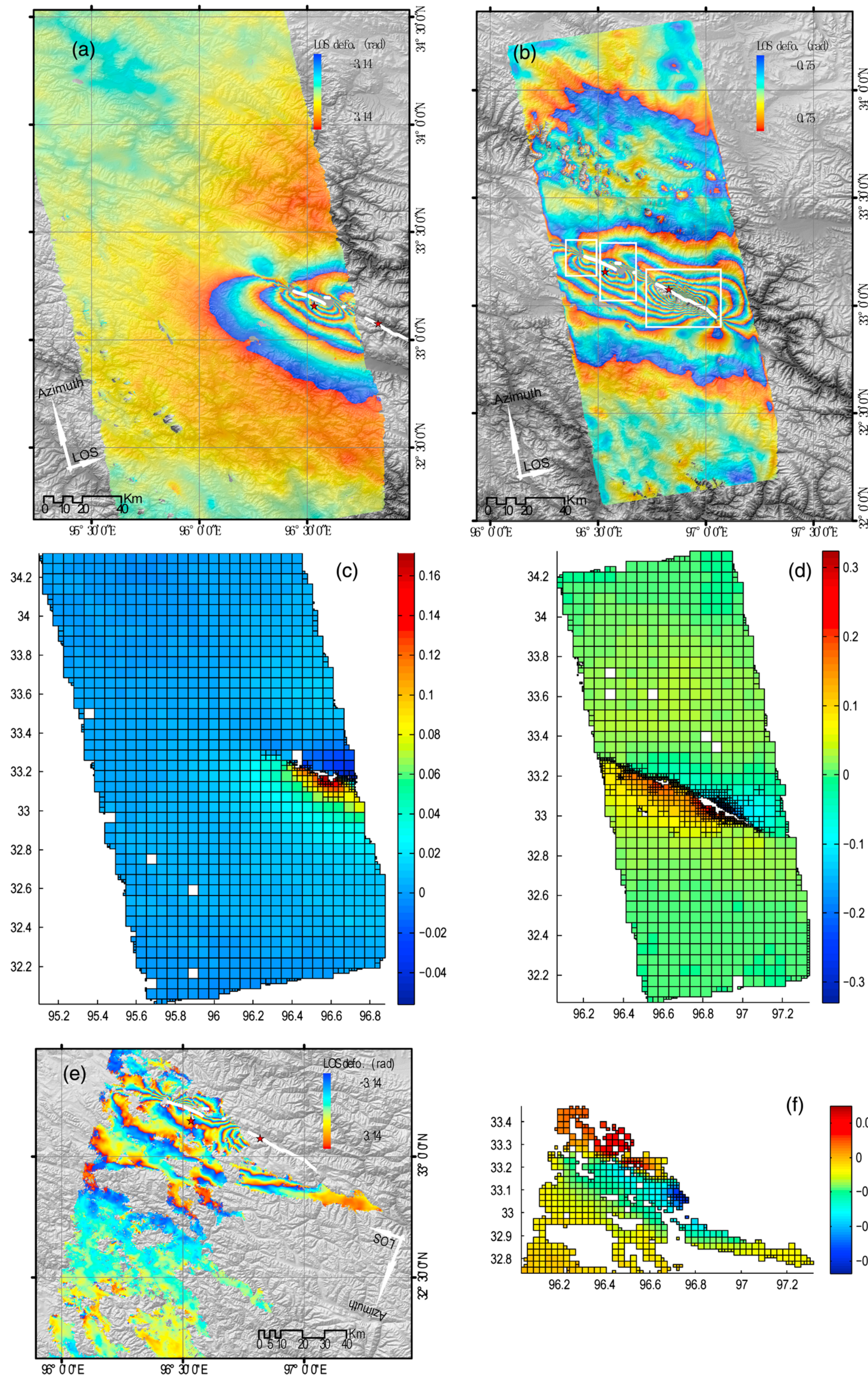

Figure 5. Rewrapped coseismic InSAR interferograms. (a) Interferogram produced using C-band Envisat ASAR data on track 498A from ESA. (b) Interferogram from L-band ALOS PALSAR data on Path 487A from Japan Aerospace Exploration Agency (JAXA). The three white rectangles indicate three areas of dense concentric fringes in the near field. Both of the interferograms are from ascending pass with right-looking geometry. The ALOS data are rewrapped into ~ −0.75 rad to 0.75 rad (~2.8 cm) so that both of the interferograms can be visually compared. The white lines and the two stars are the same as in Figure 4. (c and d) The quadtree subsampled points for Figures 5a and 5b. (e and f) The descending interferogram on track 004D from Envisat data and its corresponding subsampled points.

Table 3. Seismic Results and InSAR Data Inversion Results Using FBI Method

Segment Number	Patch Length (km)[d]	Dip (deg) East	Dip (deg) Middle	Dip (deg) West	WRSS	Seismic Moment (Nm)	Maximum Slip (m)	Relative Weights PALSAR	Relative Weights ASAR	Smoothing Factor
USGS[a]			86°N			2.50e+19				
Global CMT[b]			88°N			2.53e+19				
Two segments[c]	2.4 or 2.7	80°S		71°S	2914	1.94e+19	1.45	1.80	0.72	29
Three segments[c]	2.3, 2.5 or 2.7	82°S	73°S	76°S	2920	1.94e+19	1.57	1.79	0.73	28

[a]USGS best double couple solution with 301° strike and 32° rake angles.
[b]Global centroid moment tensor (CMT) best double couple solution with 120° strike and −13° rake angles (http://earthquake.usgs.gov/earthquakes/recenteqsww/Quakes/us2010vacp.php#scitech).
[c]InSAR data inversion results with all fault segments dipping to the south.
[d]Down-dip patch width is fixed to be 2.5 km and the different lengths correspond to the different segments.

toll of this earthquake reported on 31 May 2010 reached 2698, with 270 people missing (http://www.chinanews.com.cn/gn/news/2010/05-31/2314359.shtml). The earthquake (referred to as the "Yushu" earthquake hereafter) was recorded with a magnitude of M_w 6.9 and located at (33.224°N, 96.666°E), with a hypocenter depth of 17 km by the U.S. Geological Survey (USGS). The seismic focal mechanism of the event is consistent with slip on a vertical, ~N60°W trending, left-lateral strike-slip fault (Figure 4) (http://earthquake.usgs.gov/earthquakes/eqinthenews/2010/us2010vacp/#scitech). About 2 h before the main shock, a M_s 4.7 foreshock occurred <2 km from the main shock epicenter [*Ni et al.*, 2010].

[34] The Yushu earthquake ruptured the northwest striking, left-lateral Ganzi-Yushu fault (Figure 4), which represents the westward continuation of the Xianshuihe fault system in the eastern Tibetan Plateau. According to the field work of *Chen et al.* [2010], the surface rupture of the 2010 event is limited to between 96.77°E and 97.05°E, marked as a white line between the two green triangles on the east side (Figure 4). The most populated area in this region is Yushu-Jiegu town, just ~2 km north of the surface rupture. Proximity of the dense population to the fault rupture is the main reason for the large number of casualties in Yushu-Jiegu. Another stretch of surface rupture can be traced south of Longbao Lake [*Sun et al.*, 2010]. A right step between two parallel, left-lateral sub-segments of the Ganzi-Yushu fault constitutes a pull-apart basin and created Longbao Lake. The USGS epicenter is located close to the small basin, whereas the maximum surface offset occurred ~30 km away to the southeast.

3.2. Coseismic InSAR Data Processing and Analysis

3.2.1. Coseismic InSAR Data of the Yushu Earthquake

[35] Two different satellites acquired data over the epicentral region within a few days to a few months after the Yushu earthquake, which have optimal temporal/spatial baselines with their corresponding preseismic acquisitions and provide a good opportunity for this study. European Space Agency's (ESA) Envisat satellite acquired two pairs of C-band advanced synthetic aperture radar (ASAR) image mode data along ascending track 498A and ascending track 455A (Table 2 and Figures 5a and S2). Track 498A covers the western portion of the rupture with a perpendicular orbit baseline as small as ~12.5 m. The data from track 455A do not show useful signals at the fault location because of spatial decorrelation effects (Figure S2). A descending pass ASAR acquisition on 27 April 2010 along track 4 could have captured the coseismic deformation, but the data are corrupted and cannot be used (European Space Agency, personal communication, 2010). However, a later acquisition along track 004D on 1 June 2010 can be used with a preseismic acquisition on 3 November 2009, with a perpendicular orbit baseline of ~165.0 m and a temporal separation of ~0.58 year. This interferogram (Figure 5e) is valuable for the analysis despite its heavy decorrelation effects, because it is the only usable data collected along a descending track for the Yushu earthquake.

[36] The Japanese satellite ALOS acquired two pairs of FBS (fine beam synthetic aperture radar (SAR)) mode and two pairs of wide swath mode Phased Array Type L-Band Synthetic Aperture Radar (PALSAR) data that span the earthquake (Table 2). All of the four ALOS data pairs were processed to extract the coseismic deformation, but only the data from ascending Path 487A give satisfactory results (Figure 5b) and the interferogram covers ~90% of the coseismic deformation field. The wide swath data from the descending pass are difficult to be used for producing interferograms due to burst overlap problems [*Tong et al.*, 2010]. The interferogram on Path 138D is shown in Figure S3, and the interferometric coherence maps of the four track/path data can be found in Figures S4–S7.

3.2.2. InSAR Data Processing and Analysis

[37] We process these data with the ROI_pac software package developed at the Jet Propulsion Laboratory/California Institute of Technology [*Rosen et al.*, 2004] with an extension for processing ALOS Fine Beam Double/Single Polarisation (FBD/FBS) data and wide swath data by *Sandwell et al.* [2008]. The 3″ Shuttle Radar Topography Mission (SRTM) digital elevation model (DEM) [*Farr et al.*, 2007] is used for topographic phase removal in ASAR data processing and it is interpolated to 1″ spacing for ALOS data processing. The residual orbital phase and contributions to the signals from systematic atmospheric stratification are estimated and removed with a least squares procedure assuming a close-to-zero phase change in the far field [*Sun et al.*, 2011].

[38] The far-field regions of the data without significant deformation are carefully selected so that a long wavelength orbit ramp and atmospheric delay can be estimated and will not distort the coseismic signals in the near field. For the ALOS data in track 487A, the south-to-north coverage spans ~250 km (three standard frames) and we select the northern 32 km and southern 53 km areas as the far field. The ASAR data coverage along track 498A is ~443 km and we use the southern 15 ~ 45 km and northern 75 ~ 210 km areas as the far field (two irregular-shaped polygons, >100 km away from the fault). The track 004D data are mostly coherent in

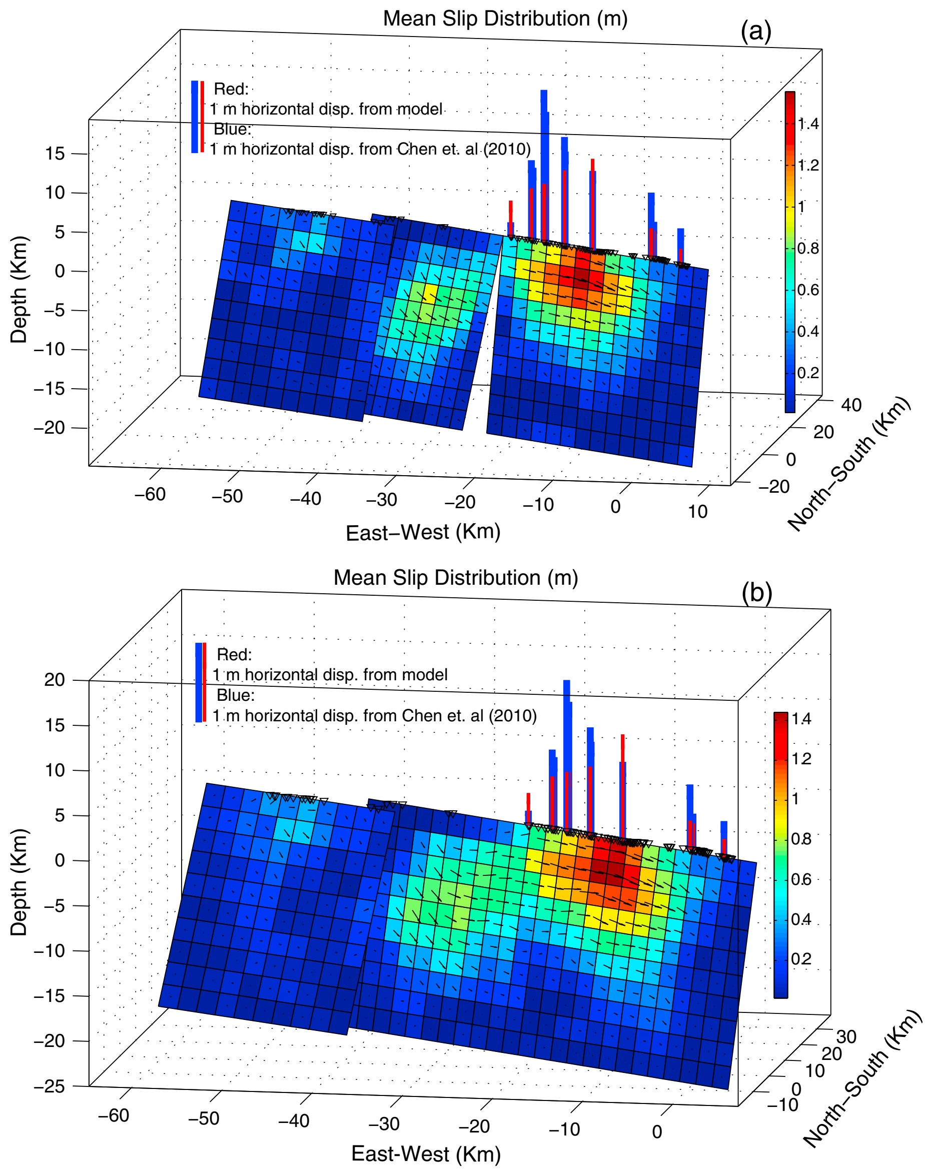

Figure 6. Slip-distribution models of the Yushu earthquake from two ascending pass InSAR data using the FBI method. (a) Three-segment fault model inversion. (b) Two-segment fault model inversion. The triangles are the field investigation points from field observations. The vertical bars represent the measured displacements (blue) in the field and the model predicted displacement (red) at the same location.

the south of the fault and a small southernmost area is selected as the far field.

[39] After the above operations, we rewrap the unwrapped interferogram of ASAR track 498A data into $-\pi \sim \pi$ radian phase cycles and ALOS path 487A data into $-0.75 \sim 0.75$ rad phase cycles, so that both of them have common ~2.8 cm LOS color cycles (Figure S8). Figures 5a and 5b show the rewrapped results, which can be visually compared in the same phase scale. Note that the incidence angle varies from 18.5° in the near range to 27.5° in the far range for ASAR data and from 36.6° to 41.6° for the ALOS data. The color cycle changes in opposite directions across the fault, reflecting the reversal of LOS motions across the left-lateral strike-slip rupture. The deformation is dominated by displacements away from the radar sensor to the south of the fault and toward the sensor to the north of the fault on the ascending pass interferograms. In the northern far-field area of the ALOS path 487A data (Figure 5b), there is an additional phase cycle observed after removing the orbital ramp. Given the large distance from the fault, we argue that this feature does not represent real deformation, but is likely caused by contributions from atmospheric water vapor phase delay during the PALSAR observations.

[40] We note three areas of dense concentric fringes in the near field of the ALOS data (the three rectangles in Figure 5b), which are within 15 km perpendicular distance from the fault. One is around the main rupture (white line) mapped in the field [*Chen et. al*, 2010] with the right red star close to its center identifying the location of peak surface slip. The second fringe concentrated area is located around Longbao Lake (Figure 4), where a secondary surface rupture was mapped to the south of the small basin and some small fissures were found to the north of the lake [*Chen et. al*, 2010]. Between these two areas of maximum range-change

Table 4. Parameters From the Three-Step MAP Inversion of the Three InSAR Data Sets of the Yushu Earthquake

Model Number	Dip (East)	Dip (Middle)	Dip (West)	Sigma1 (P487A)	Sigma2 (T498A)	Sigma3 (T004D)	Smooth Factor	Maximum Slip (m)	Maximum Posterior PDF	WRSS	Figure No.
Parameter bounds	60° N ~ 90°N	60°S ~ 90° S	60° S ~ 90°S	0.1 ~ 20	0.1 ~ 20	0.1 ~ 20	1 ~ 100				
Initial values	75°N	75°S	75°S	1.0	1.0	1.0	25.0				
Step 1	89.8°N	79.5°S	81.9°S	7.23	10.4	11.20	25.5	1.39	−7605	3348	7a
Step 2	89.7°N	81.9°S	79.4°S	7.28	9.91	10.88	49.6	1.39	−7402	3495	7b
Step 3	89.7°N	81.9°S	79.4°S	7.28	9.98	11.06	59.7	1.38	−7337	3530	7c

gradients, the fringes change more gradually and no surface ruptures were found in the field [*Chen et. al*, 2010]. This indicates that the fault slip did not propagate to the surface along the central portion of the rupture. To the west of Longbao Lake, the secondary rupture continues for ~7.3 km and forms a third small area of high range-change gradient at which all fringes converge. Figure 5a shows the ASAR sensor observation of the coseismic signals along track 498A. As both of the ascending pass observations are with right-looking geometry, the fringe patterns of the two interferograms (Figures 5a and 5b) are very similar and the PALSAR range change is only slightly larger than the ASAR range change due to the larger contributions to the LOS displacements from horizontal deformation (Figure S8). The interferogram on track 004D suffers from heavy decorrelation effects (Figure 5e), but it can be used to better constrain the fault geometry of the western rupture segments, especially the two parallel branches on the two sides of Longbao Lake, due to its different view angle from the descending orbit pass.

[41] Prior to modeling the data, we use the quadtree decomposition method [*Jonsson et al.*, 2002] to resample the PALSAR and ASAR data into 1602, 1347, and 588 points, respectively (Figures 5c, 5d, and 5f). We sample the InSAR interferograms both in the near field and the far field, so that the observations can be used to better constrain the fault slip on the shallow and deep rupture simultaneously and the inversion does not overestimate/underestimate the seismic moment. We account for the variable LOS unit vectors across the SAR images due to their different incidence angles.

3.3. InSAR Data Inversion Using the FBI Method and the Three-Step MAP Method

[42] Before proceeding with the inversion of the InSAR deformation data for coseismic fault slip, we consider the geologic field investigation data to constrain the surface trace location of the Yushu earthquake rupture [*Chen et al.*, 2010]. We find that the surface trace is composed of at least three primary strands, namely, (1) the surface rupture segment between the eastern two green triangles (Figure 3) near which the heaviest damage occurred, (2) the western extension of the surface rupture along the northern shoreline of Longbao Lake where small fissures appeared and little fault slip reached the surface, and (3) a rupture segment on the south side of Longbao Lake with observable slip on the ground surface [*Sun et al.*, 2010]. The fault trace is offset by ~4.5 km across Longbao Lake to form a pull-part basin. We refer to the three sections as the eastern, middle, and western segments. The entire extent of surface rupture is ~67 km long, as is delineated by the white lines in Figure 4, including the blind part between the two areas of large range-change gradient. In addition, we find two bedrock fault scarps (two blue points in Figure 4), which suggest that the eastern segment dips steeply to the north and the middle unruptured segment along the north shore of Longbao Lake dips to the south (Figures 4b and 4c). The field evidence thus suggests that the fault can be modeled with three segments from southeast to northwest and that fault dip varies along strike. To fully explore the fault model parameter space, we design the inversion process with either three segments following the field investigation, or two segments of which one is a combination of the eastern and middle segments of the fault. In addition, in order to investigate the role of spatially correlated noise in the model inversion, we use both a diagonal covariance model and a full covariance model [*Sun et al.*, 2011; *Sun et al.*, 2008] of InSAR data and compare the final slip solutions. The top edges of the fault segments are linear and approximated to follow the geologically mapped fault surface trace as closely as possible. Small variations are ignored, especially at the eastern end of the main surface rupture (Figure 4).

3.3.1. Slip Distribution Using the Fully Bayesian Inversion Method and High Quality InSAR Data Only

[43] First, we invert for the slip distribution using the FBI method originally developed by *Fukuda and Johnson* [2008] with various changes to accommodate the InSAR data and its errors. It solves simultaneously for the slip distribution, smoothing factor, relative data weights, and unknown fault dips because the surface location of the seismogenic fault is well established from the field and InSAR data. In this case, we use only the high quality data on path 487A (ALOS) and track 498A (ASAR). These two data sets were acquired very soon after the earthquake without significant postseismic deformation signals included. We see little evidence for random noise and unwrapping phase jumps, except for a number of apparent spatially correlated errors, such as the feature seen north of 33.5°N on Figure 5b. In the inversion, we constrain the fault slip to be left-lateral strike slip, but provide no constraint on the dip slip component. We grid the fault segments into 340 patches with ~2.5 × 2.5 km dimension and the down-dip fault width is fixed to be 25 km. Table 3 shows the inverted parameters from the teleseismic inversion and the two- and three-segment InSAR data inversions using FBI method.

[44] The end points of the top edges of the fault segments at the surface are marked as green triangles in Figure 4. The surface traces in the two cases are the same except that the eastern two segments are combined to form one segment with uniform dip in the two-segment case. The Weighted Residual Sum of Squares (WRSS) in the two cases have negligible difference and other parameters, such as the smoothing factors, the relative

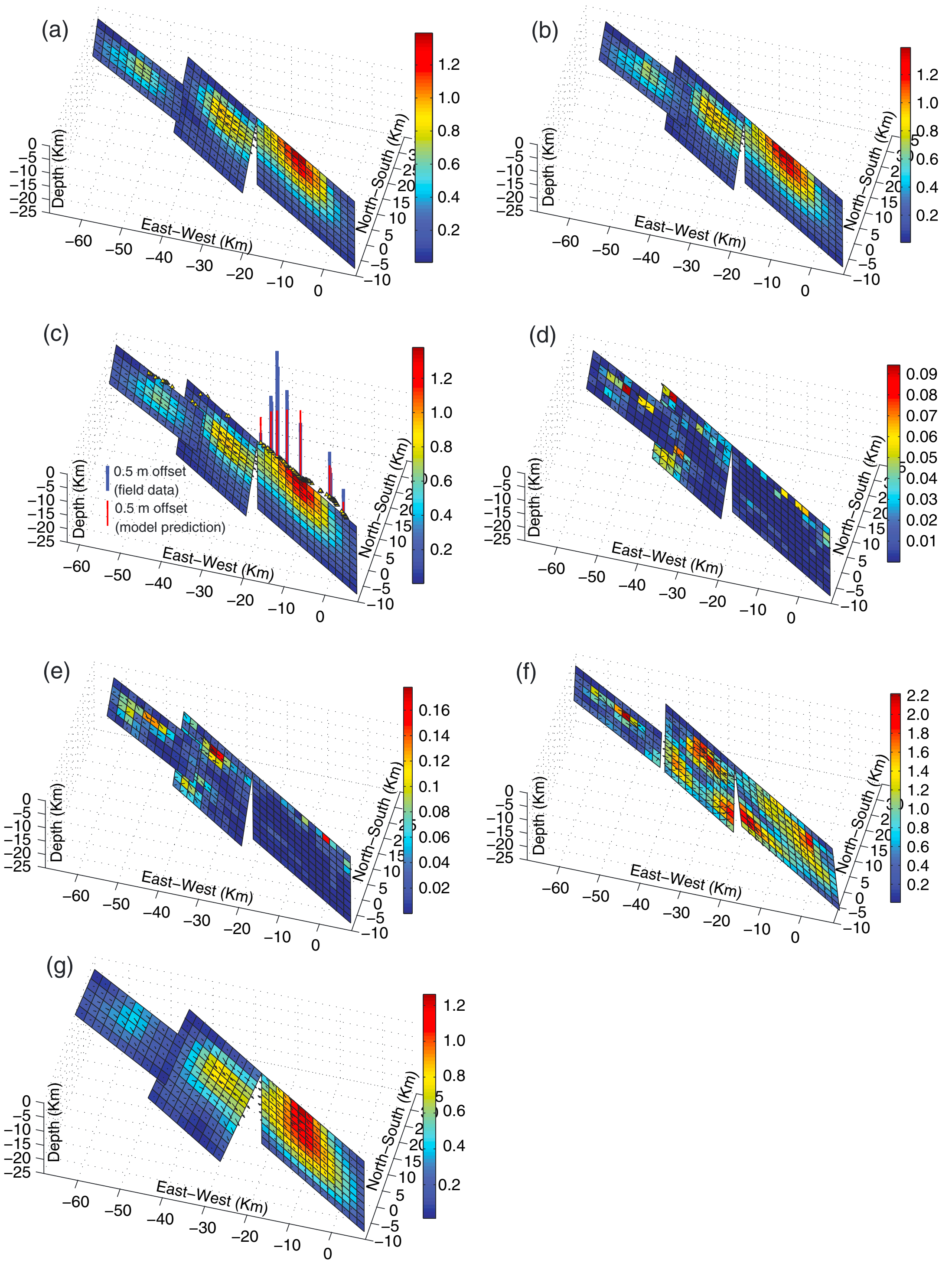

Figure 7. Slip-distribution models of the Yushu earthquake from two ascending and one descending pass InSAR data using the three-step MAP inversion method. (a–c) The models from the first, second, and third steps of the MAP inversion, respectively. The vertical bars in Figure 7c represent the measured displacements (blue) in the field and the model predicted displacement (red) at the same location using the three-step MAP inversion method. (d) The difference between the models from the first and second step of the MAP inversion. (e) The difference between the models from the first and third step of the MAP inversion. (f) The model from the first step of the MAP inversion without slip constraints applied. (g) The model from the first step of the MAP inversion with diagonal covariance model applied.

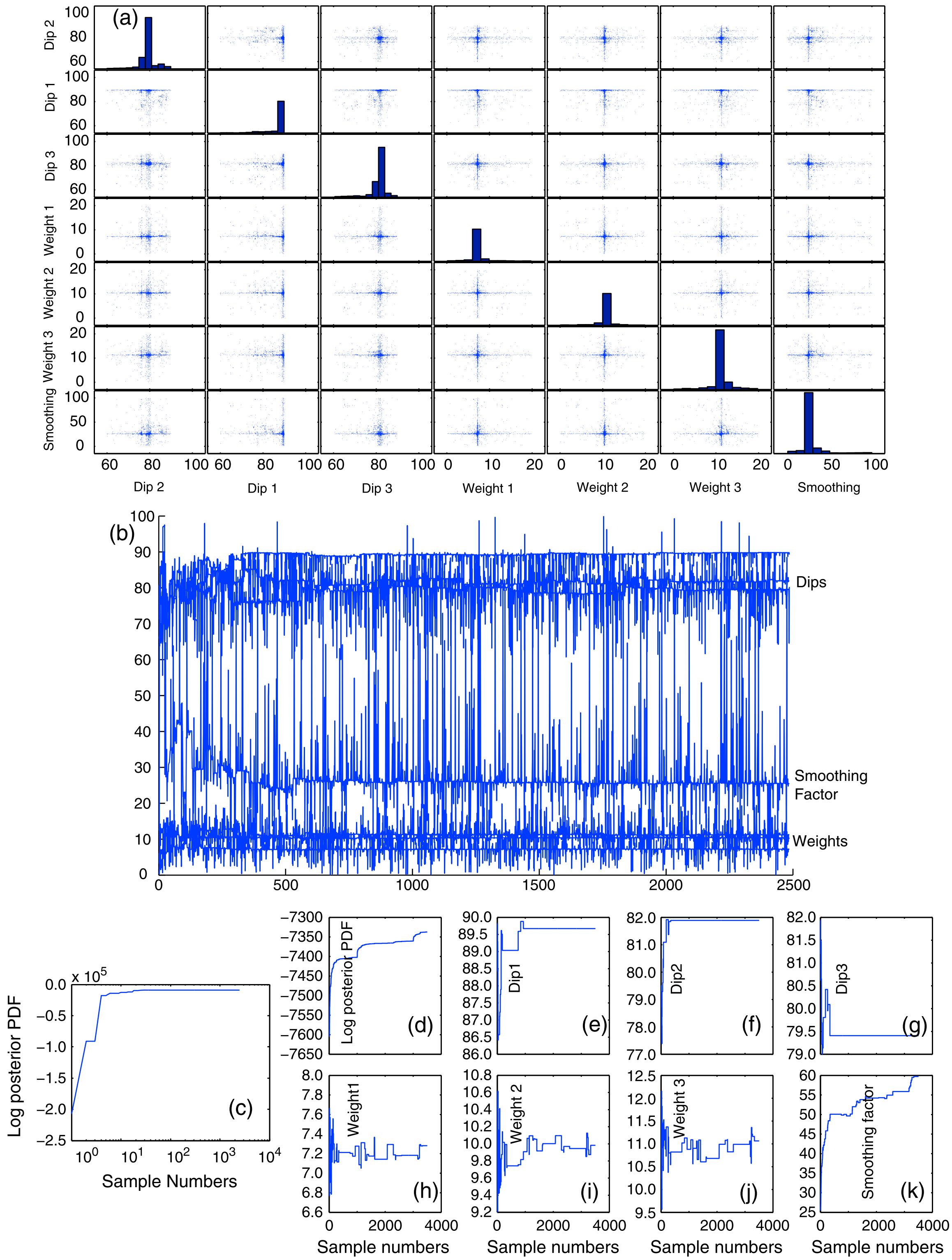

Figure 8. The evolving parameters of the Yushu earthquake model from the three-step MAP inversion. (a) The scatterplots of the nonlinear parameter pairs from the first step of the MAP inversion. (b) The seven evolving parameters of the first step of the MAP inversion. (c) The evolving posterior PDF (in logarithm) of the first step of the MAP inversion. (d–k) The evolving posterior PDF (in logarithm) and seven parameters of the second (0–1000 samples) and third steps (1000–3500 samples) of the MAP inversion.

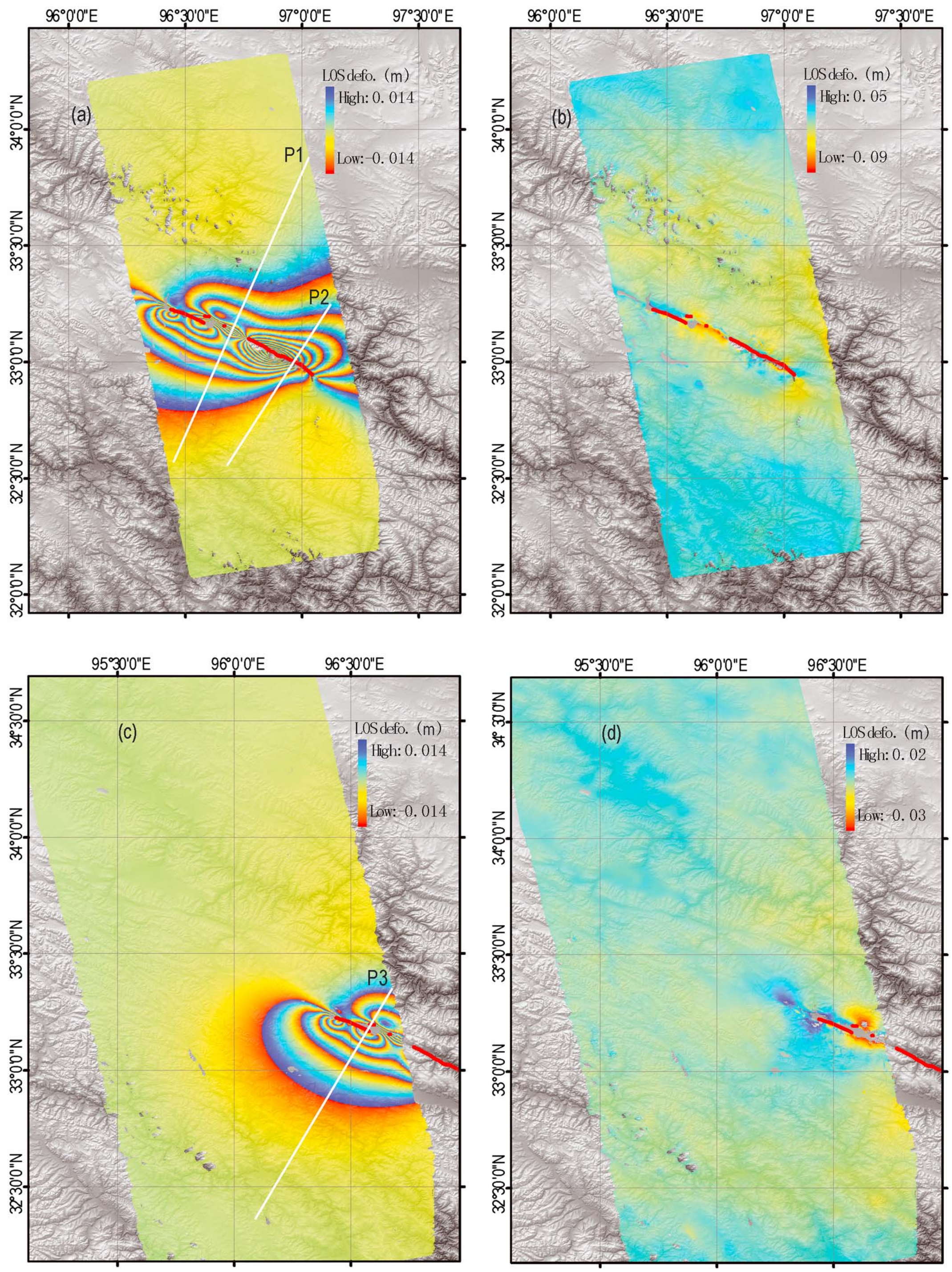

Figure 9. InSAR interferogram forward modeling and its residual using the fault model in Figure 7c. (a and b) ASAR interferogram forward modeling on track 498A rewrapped into $-0.014\,\mathrm{m} \sim 0.014\,\mathrm{m}$ cycles and its residuals. (c and d) PALSAR interferogram forward modeling on path 487A rewrapped into $-0.014\,\mathrm{m} \sim 0.014\,\mathrm{m}$ cycles and its residuals. (e and f) ASAR interferogram forward modeling of track 004D data rewrapped into $-0.014\,\mathrm{m} \sim 0.014\,\mathrm{m}$ cycles and its residuals. The red lines are the fault trace from field investigations. The white straight lines are the locations of four profiles in Figures 9g–9j across the fault. (g–j) The four profiles P1, P2, P3, and P4 in red color from the model predictions, with the corresponding observations in black color, respectively. Note the profiles are plotted from the north to the south.

data weights, and the total seismic moment released, are also similar (note that only the diagonal terms in the data covariance model are used here) (Table 3). The two inversions are completely independent but use the same InSAR data sets. The seismic results show a near vertical fault steeply dipping to the north ($86° \sim 88°$). The geologists found that the eastern segment has a north dip angle as small as ~65° (L. Chen and B. Fu, personal communications, 2010). However, in both

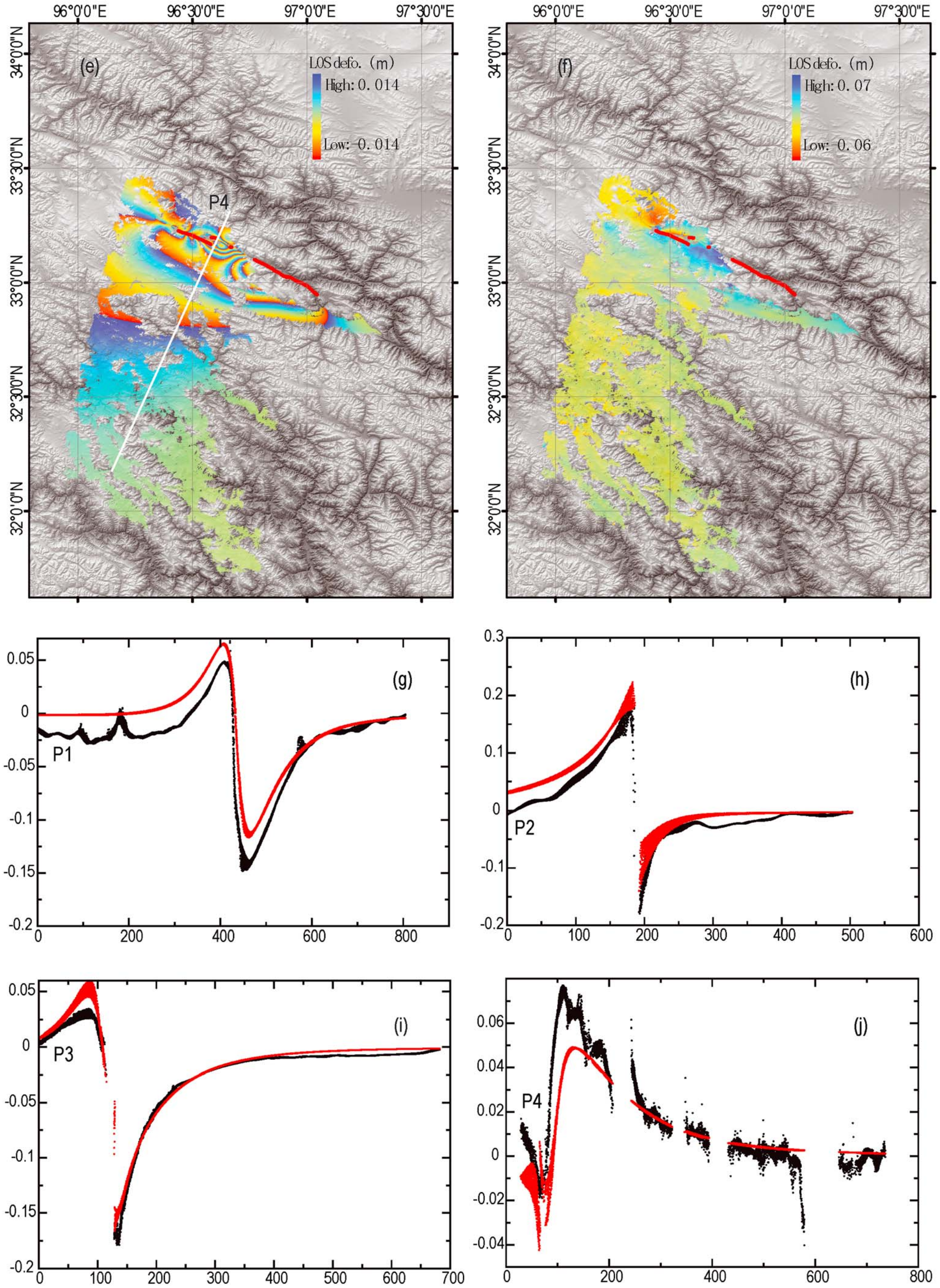

Figure 9. (continued)

InSAR inversions, all the fault segments are found to be dipping to the south (Table 3). The maximum slip is 1.45 m in the two-segment case and 1.57 m in the three-segment case, and the difference may indicate minor trade-offs between the fault dip and fault slip or may be related to the different smoothing constraints as described below.

[45] Figure 6 shows the fault slip distribution of the two cases. In general, the results show very similar slip distributions independent of which segmentation scheme is used or which dip angles are inverted for. The most significant slip occurs at $0 \sim 10$ km depth in between ~ -5.0 km and ~ -25.0 km along strike (reference point at 33°N, 97°E). The surface slip-distribution pattern of the fault models is generally consistent with the field observations which found substantial offsets near the Yushu-Jiegu town (eastern segment), no visible slip along the central segment [*Chen et al.*, 2010], and some small slip features on the western segment south of Longbao Lake [*Sun et al.*, 2010]. The inversion result indicates that the maximum slip is close to the surface at around ~2.5–5.0 km depth near the town of Yushu-Jiegu, which is consistent with the near-field deformation pattern showing that the interferogram fringes there get closer in spacing (Figure 5). The central segment in Figure 6a or the western portion of the eastern segment in Figure 6b shows a

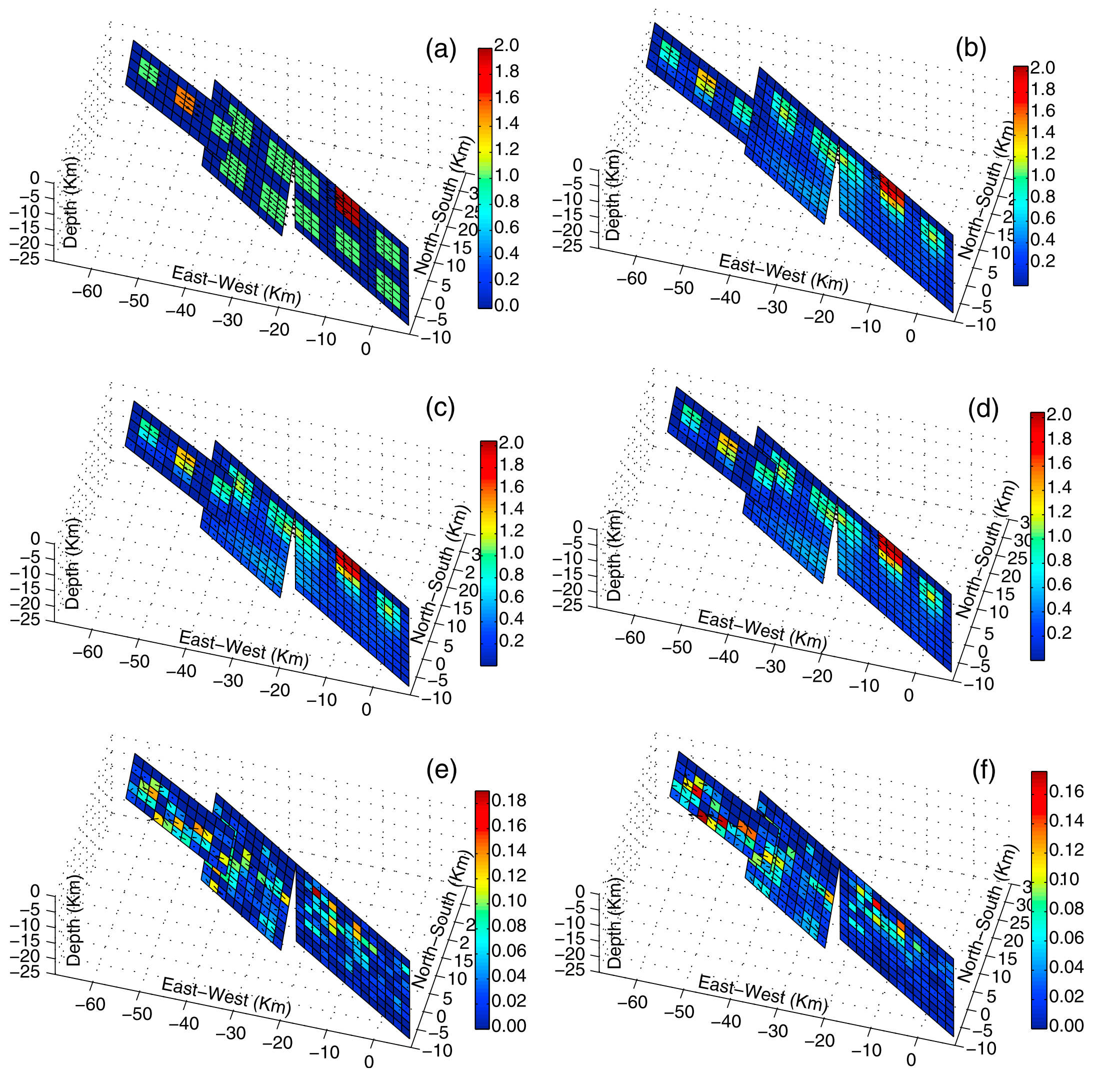

Figure 10. Checkerboard model and the inverted models using the three-step MAP inversion method. (a) Checkerboard model with the fault geometry adopted from Figure 7c. (b–d) The models from the first, second, and third steps of the MAP inversion, respectively. (e) The difference between the models from the first and second steps of the MAP inversion. (f) The difference between the models from the first and third steps of the MAP inversion.

secondary slip peak at ~5.0 km depth, but its magnitude is only ~0.9 m, much smaller than that of the first one and there is almost no slip near the surface. The field survey found no surface rupture but only small fissures at two places in the region (see the open triangles in Figure 6 for surface offset locations). The western segment shows a third peak slip of ~0.6 m at shallow depth with some slip reaching the surface. A follow-up field investigation confirmed the existence of the surface trace along this segment [*Sun et al*., 2010]. There is a small (<0.36 m) dip-slip component in the slip-distribution solutions, but no vertical motion can be established on the ground [*Chen et. al*, 2010]. We prefer the three-segment model based on two points: (1) The field data show the middle and eastern segments having different dip angles (Figures 4b and 4c), and (2) the slip-distribution results show obvious changes between the middle and eastern segments (surface ruptured or blind) in the three-segment case and the two portions (the eastern and western parts) of the eastern segment in the two-segment case.

3.3.2. Slip Distribution Using the Three-Step MAP Inversion and All Three InSAR Data Sets

[46] The inversion results from the FBI method show acceptable models with good fitting to the high quality InSAR data which were acquired quickly after the earthquake. However, a discrepancy exists between the inverted fault dips and that inferred from geological observations. In order to investigate the origin of the problem and better constrain the fault geometry, we combine a noisy ASAR interferogram from a different view angle (track 004D).

[47] We adjust the inversion as follows: (1) using both the descending and ascending pass data to better constrain the fault geometry and reduce the trade-off effects between fault slip and fault dip; (2) using the full covariance model [*Sun et al*., 2011; *Sun et al*., 2008] to accommodate the spatially correlated errors of InSAR data and investigate its influence on the fault geometry and slip inversions; (3) reducing the fault plane width of the western segment to save computation time; and (4) applying a new smoothing scheme in the three-

Table 5. Parameters From the Three-Step MAP Inversion of the Three Predicted InSAR Data Sets Using the Checkerboard Model

Model Number	Dip (East)	Dip (Middle)	Dip (West)	Sigma1 (P487A)	Sigma2 (T498A)	Sigma3 (T004D)	Smooth Factor	Maximum Slip (m)	Maximum Posterior PDF	WRSS	Figure No.
Parameter bounds	60° N ~ 90°N	60°S ~ 90° S	60° S ~ 90°S	0.1 ~ 20	0.1 ~ 20	0.1 ~ 20	1 ~ 100				
Initial values	75°N	75°S	75°S	1.0	1.0	1.0	25.0				
Step 1	89.9°N	80.5°S	78.7°S	1.27	1.35	1.26	10.4	2.04	−1332	3230	10b
Step 2	89.9°N	80.5°S	78.0°S	1.08	1.21	1.11	11.1	2.04	−1051	3636	10c
Step 3	89.9°N	80.5°S	78.0°S	1.09	1.14	1.18	12.5	2.04	−1006	3622	10d

segment case (only this configuration is considered in the inversion hereafter) to avoid artificially over-smoothing at the segment boundary, so that the middle and eastern segments can be smoothed together, because there is no sharp change in the SAR interferogram here.

[48] We try to combine the descending pass data in track 004D with the ascending pass observations used in the FBI method, but the FBI method leads to a very rough slip distribution and has difficulties to converge after a large number of iterations. This is because the FBI method falls in low probability regions maybe due to a large parameter step size adopted in the inversion (Figure S9a). For comparison, Figure S9b shows the two ascending pass data inversion process in section 3.3.1, where the logarithm posterior PDF reaches a stable value of ~ -50 after ~6000 iterations and we discard the first 6000 models (the burn-in samples) and use the other models as the effective posterior PDF sampling.

[49] By following the four points listed above, we carry out the Yushu earthquake data inversion using the new three-step MAP inversion method using all of the three data sets acquired both in descending pass and ascending pass. Based on the experiences in the verification test in section 2.4, we implemented the three-step MAP inversion on the real InSAR data sets with full covariance model applied in the inversion. The three steps are implemented sequentially, and the result of every step inversion is presented for comparisons. Because the Yushu earthquake is nearly a pure strike-slip event, the bounds of the net slips and rake angles are set to be [−10 m,10 m] and [−30°, 30°], respectively. In order to test the usefulness of the slip constraints in this inversion, we implemented another independent inversion removing these slip constraints. We adopted the three-segment configuration for the fault model inversion, with the east segment dipping to the north and the other two segments dipping to the south. In addition, the model with the east segment dipping to the south is also tested, and the result shows that its dip angle is almost the same as that in the former case of 90.0°. The nonlinear parameter bounds adopted in the Yushu earthquake inversion are shown in Table 4.

[50] In the first step of the MAP inversion, the ASA inversion generated 2486 models, among which 320 models are accepted. In every model generated, the nonlinear parameters are sampled once within respective bounds, and the slip distribution is inverted for using the least squares method without positivity constraint. If some of the inverted slip vectors exceed their valid bounds we assigned in advance, they are replaced with the slip bound values (net slip and/or rake). The number of generated models and accepted models can be set before the ASA inversion, and the inversion can also be stopped at any time by monitoring the output of the ASA inversion. The inversion results are listed in Table 4 and the slip distribution of the inversion is shown in Figure 7. We generated only 2486 models because the posterior PDF already becomes stable after the first 100 models, and the nonlinear parameters become stable after ~600 models (Figure 8). The total number of generated models is selected to be large enough, so that the nonlinear and linear parameters (or slip vectors) all become stable in the inversion.

[51] Figures 7a–7c are the models from step-one, step-two, and step-three MAP inversions, respectively. The basic features of the output model from each step of the inversion are quite similar. The differences between the first and the second steps of the MAP inversions (Figure 7d), or between the first and third steps of the MAP inversions (Figure 7e), mainly concentrate around the area without strong constraint from InSAR data. Along the Yushu earthquake fault, the western and deeper parts of the middle segment and the west segment show some differences, which can be as large as 9.0 ~ 17.0 cm (Figures 7d and 7e). There are also minor differences near the surface at the east segment due to loss of InSAR coherence here. The final model in Figure 7c shows that the slip distribution on the three segments (namely the east, middle, and west segments) is quite different. Most of the important slip occurred on the east segment, where strong ground motion and damages were observed in the field [*Chen et.al*, 2010], and the maximum slip is located just at the surface, while the maximum slip does not reach the surface in the FBI results. Substantial slip also occurred on the middle segment, but the slip magnitudes are dramatically smaller than on the east segment. Furthermore, the slip on the middle segment was completely blind and does not reach the surface. On the west segment, slip values are less than on the middle segment, but with a small amount of slip propagating to the surface.

[52] In another test using the first step of the MAP inversion, but without slip constraints applied, we found that the optimized model is quite different from the model inverted using the slip constraints (Figure 7f). The model shows complex slip behaviors on every segment, and there are a large number of slip reversals on the deeper part of the middle segment. We do not think the model is reasonable for the earthquake rupture because it violates our knowledge of the kinematics of the left-lateral strike-slip fault, though the data fitting of this model is good, and its posterior PDF is also larger than that of the model in Figure 7c. Therefore, we discard this model and adopt the one with positivity slip constraints as our preferred model (Figure 7c). The inversion also indicates the importance of the slip constraints in the MAP inversion. In the verification test in section 2.4, we implemented a similar test, but the slip distribution models have insignificant differences there. This indicates the

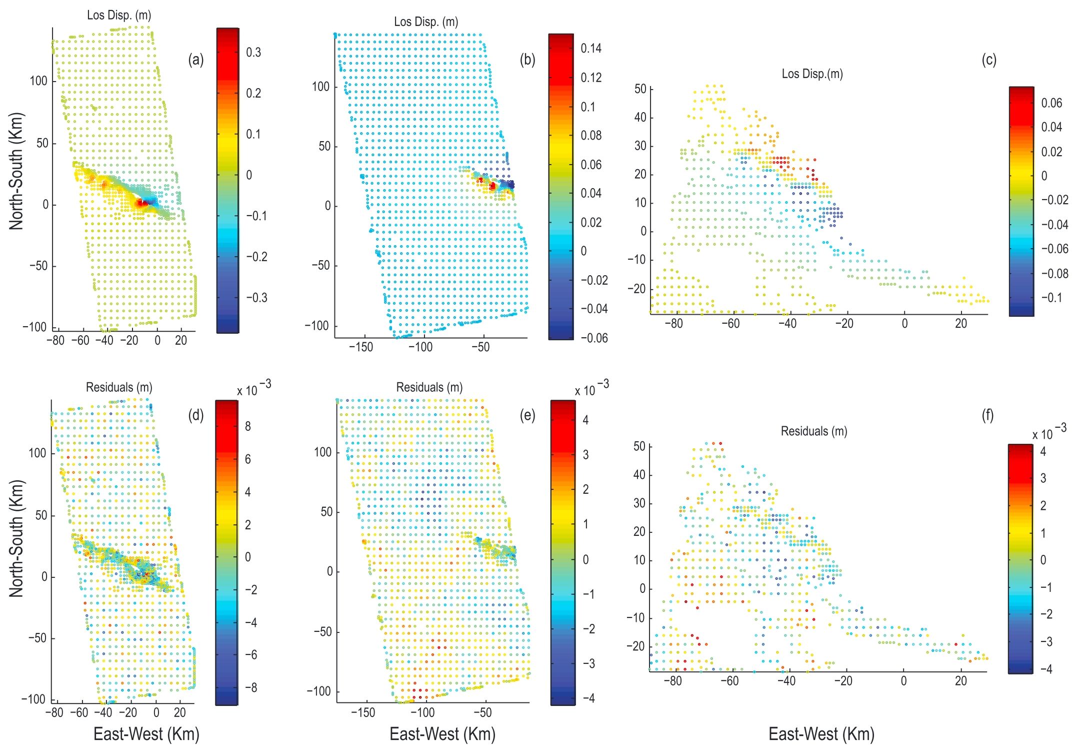

Figure 11. (a–c) Predicted InSAR data on track 498A (ASAR), path 487A (ALOS), and track 004D (ASAR), respectively, using the checkerboard model in Figure 9a and (d–f) corresponding inversion residuals.

complexity of the parameter space structure in different cases, and using the slip constraints would always be advisable since we have little knowledge about the parameter space explored.

[53] In order to test the influence of the covariance model on the three-step MAP inversion, the inversion with diagonal covariance model is also tested. In contrast to the verification case, where the different covariance models have insignificant influences on the results, we see that the fault geometry parameters are quite different for the two cases, even though the slip-distribution models are quite similar (Figures 7c and 7g). Two dip angles inverted with the diagonal covariance model reached their lower bounds, and the relative weights of the data sets are also much smaller than for our preferred model. The inversion result suggests that consideration of the full covariance model may be necessary in some cases, especially when InSAR data with significant spatially correlated noise are used, such as in the ALOS 478A interferogram we used in this study (Figure 5b).

[54] We also provide the distribution of the seven nonlinear parameters in the three-step MAP inversion. Their final values are well determined by the large cross points in the parameter-pair matrix (Figure 8a), except for the dip angle of the east segment (Dip 1), which reaches the upper bound of 90°. The other parameters are well distributed within their respective ranges. Figures 8b and 8c show the evolving values of nonlinear parameters and posterior PDF of the first step of the MAP inversion, and Figures 8d–8k show the corresponding evolution parameters in the second and third steps of the MAP inversions. Note that the posterior PDFs between Figures 8c and 8d have different values due to their different posterior PDF equations.

[55] The forward modeling results based on our preferred model (Figure 7c) using the three-step MAP inversion are shown in Figures 9a, 9c, and 9e. We again show the maps in wrapped LOS fringes in 0.028 m cycles for the interferograms from the different radar wavelength systems. Their corresponding residuals are shown in Figures 9b, 9d, and 9f with unwrapped values. In order to objectively evaluate the inversion residuals and make the color bar presentation more easy to read, we used a cumulative density function to evaluate the residual distribution and excluded few points (outliers) of residuals larger than or smaller than a designated threshold (Figures S10a and S10b). There are no systematic residuals found in the three residual maps (Figures 9b, 9d, and 9f). An important error source is the spatially correlated noise on Figure 9b, mostly to the north of the fault on path 487A (the yellow area). This appears to be the atmospheric signals we found in the observation (Figure 5b), which are as large as ~0.025 m. This residual is also manifested in the two profiles P1 and P2 in Figures 9g and 9h, where the profiles from the observation and the model prediction have a ~0.025 m difference. This indicates that the large-scale atmospheric phase screen is not interpreted as earthquake deformation in our model. The other residuals from the two high-quality interferograms (Figures 9b and 9d) are mostly concentrated in the near field, and it is normal that the complexity of coseismic deformation distribution near the fault cannot be well interpreted by a simple elastic model relying on rectangular dislocation planes. The residuals on track 498A (Figure 9d) near the fault share the same LOS directions on both sides of the fault. These small residuals cannot be interpreted by our model for this pure strike-slip fault, and they may be attributed to other non-tectonic origins. The residuals on track 004D (Figure 9f) are larger than the residuals

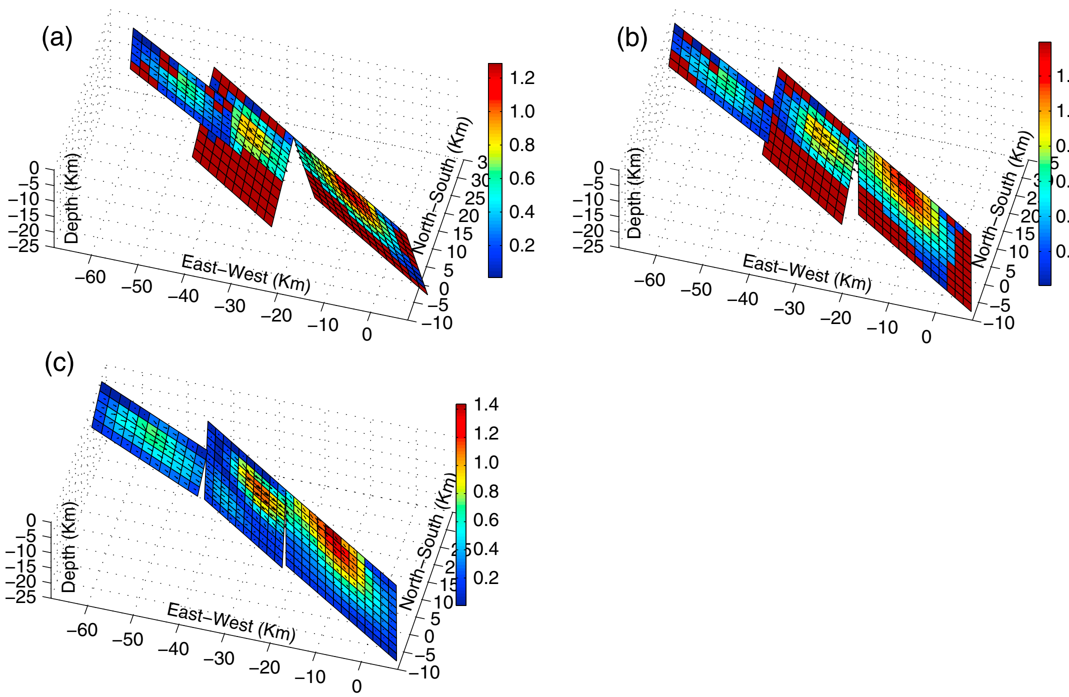

Figure 12. (a) Slip-distribution model of the Yushu earthquake from the first step of the MAP inversion, on which the patches with the slip-replacement operation applied are highlighted with dark red color (without arrows) after the first 30 models. (b) Same as in Figure 12a but after the generation of 2486 models. (c) Slip-distribution model of the Yushu earthquake from the first step of the MAP inversion, with the smoothing factor reaching its lower bound and the slip constraint removed.

on the other two interferograms due to the following two factors: (1) The data have low coherence and thus are contaminated by random noise and typical InSAR phase unwrapping errors and (2) the post-earthquake data are acquired ~45 days after the earthquake and include early stage postseismic deformation. We do not find equivalent residuals on the ascending pass data. The profiles P3 and P4 show the differences between the observations and model predictions of the track 498A and track 004D data. Though the near-field residuals are as large as ~0.025 m, the profile variations from the near field to the far field are very similar and suggest that the model can explain the InSAR observations well.

3.3.3. Resolution Test With a Checkerboard Model

[56] In order to test the performance of the three-step MAP inversion method at the example of the Yushu earthquake investigated in this study, we design a checkerboard model using the inverted fault geometry given in Figure 7c and Table 4, and the observation point distribution and full covariance model established from the real radar data of this study. The resolution tests partly depend on the fault geometry, the designed slip model, and the InSAR data distribution, but also generally reflect the performance of the developed algorithm. If the method is used elsewhere, it is necessary to design a specific resolution test as demonstrated here.

[57] In the test, we design a slip-distribution model (Figure 10a), with two rows of slip patches distributed at different depths on the three fault segments. The slip patches are placed both in the shallow crust (<10 km depth) and the middle/lower crust (>15 km depth) (Figure 10a), so that we can test if the slips can be well recovered at different depths in the inversion process. Following the real inversion process in section 3.3.2, we invert the predicted InSAR data sets to recover the designed slip pattern using the three-step MAP inversion method. The three slip-distribution models from the three-step MAP inversion are shown in Figures 10b–10d. As in the verification test and the real InSAR data inversion, the three models have small differences (the maximum slip difference is about 16.0 ~ 18.0 cm), and most of the differences occurred on the deeper parts of the fault (Figures 10e and 10f), where the data constraints may be weak. The parameters involved in the inversion are listed in Table 5. We used the same parameter bounds (including both nonlinear and linear parameters) and initial values as in the real InSAR data inversion of the Yushu earthquake for the three-step MAP inversion. We generated 1713 models in the first step, and among which 141 models are accepted. The fault dip angles are inverted to be within 1.0° difference of the input model. This is partly because the noise in the synthetic data sets is only at millimeter level, and the covariance model used in the inversion is known, and there is no other long-wavelength noise in the data, such as the typical orbit ramp errors and large-scale atmospheric signals in InSAR data. The slip-distribution model from the first step of the MAP inversion shows that the slips on the upper row of patch groups are well recovered, but the slips on the lower row of patch groups cannot be well resolved due to the low resolution of the data for the deeper and weak slip signals there. In addition, if the slips on the upper row of patch groups are removed, the lower part zones can be recovered, though the inverted slip pattern is not as good as that of the upper row. The predicted InSAR data sets are shown in Figures 11a–11c, and the residuals of the three-step MAP

inversion are shown in Figures 11d–11f. The residuals are similar to the noise we applied to the predicted data. In addition, the relative weights of the three data sets are all ~1.0 (Table 5). This indicates that the full covariance model we used is known, and there is no other noise, such as the long-wavelength orbit ramps or atmospheric noise of InSAR data, involved in the data. However, in the real InSAR data inversion, the weights are always larger than 1.0 due to the fact that a correct full covariance model cannot be guaranteed, and the inclusion of relative weights in the inversion is always necessary.

4. Discussion

4.1. The Importance of the Slip-Replacement Operation in the First Step of the MAP Inversion

[58] In section 2.2, we introduce the procedures of the three-step MAP inversion method. In the first step, the strategy is similar to that implemented in the MBI method, in which the posterior PDFs of nonlinear and linear parameters are separated and the two kinds of parameters are solved with different methods. The MBI method uses the MCMC sampling method for nonlinear parameter inversion, and the three-step MAP method uses a highly efficient global optimization algorithm for this purpose. The two methods are different mainly on their efficiency because their posterior PDFs are the same. However, in the MAP inversion, we apply a slip-replacement operation after the least squares slip inversion, when the inverted slip vectors fall outside of the specified ranges. We highlight those fault patches with the slip-replacement operation applied at the start and end of the first step inversion, so that their number and locations can be shown. In Figure 12a, we show the result of the first step of the MAP inversion after generating 30 models. It is not a convergent model at this stage according to the evolving parameter values (Figure 8b), where the parameter variations are not stable yet. The fault geometry is different from the final model in Figure 7c, though the slip distribution is quite similar to it. The dark red patches without arrows are those for which the slip-replacement operation is applied at this stage (Figure 12a). We find that those patches, such as the five rows of patches at the bottom of the middle segment, are located around the patches with significant slips we described in section 3.3.2. The areas with the slip-replacement operation applied are not well constrained from the InSAR data used here. At the end of the first step of the MAP inversion after the generation of 2486 models, the distribution of the patches with slip-replacement applied is similar to that in Figure 12a, but their number is decreased (Figure 12b), such as the four rows of patches at the bottom of the middle segment. The net slips of these patches are less than 0.1 m, compared with the significant slips on our final model in Figure 7c, so that they have no important influences on the posterior PDF computation. However, the slip-replacement operation is important in that it prevents the optimization from sampling the large posterior PDF regions with unphysical slips. Therefore, a model that is compatible with the physics and tectonic style of a particular earthquake rupture can be obtained in the parameter space. It has been demonstrated that the slip model can be very different with our preferred model (Figure 7c) when the slip bounds are removed (Figure 7f).

[59] In addition, a quantitative criterion, to judge if the changes by the slip-replacement operation are significant or not, is to compute the associated seismic moment in every iteration. This is a simple linear operation and does not need large CPU cost. We computed the ratio of the seismic moment change introduced by the slip-replacement operation to the total seismic moment in the Yushu earthquake inversion and find that the ratio is far less than 1%. Our tests also show that the posterior PDF with slip replacement has very little decrease because the slip replacement prevents the data noise from being fitted by slip reversals, while the posterior PDF is always kept at the same level after convergence (Figures S11 and S12).

[60] It is also possible to constrain the smoothing factor with some suitable bounds for this purpose, while without using the slip-replacement operation, so that the final model is objectively smoothed and the globally optimized model can be obtained. In another inversion test, we set the bounds for the smoothing factor to [20.0, 50.0] after a series of tests. It is easy to get an optimized model as in Figure 12c from the first step of the MAP inversion, and the smoothing factor reached the lower bound of 20.0 in this case. The final model is similar to our preferred model in Figure 7c; however, the fault geometry and the maximum slip are obviously different from it. There are some areas with large slip reversals that occurred in the lower west corner of the middle segment in this model (Figure 12c). It is obvious that this is not a satisfactory model for the earthquake even though it captured the main features of the rupture. Because we never know a suitable smoothing factor in advance, the objective smoothing of a slip solution cannot be guaranteed. It is selected by trial and error in the test, but can be determined objectively in the FBI method and the three-step MAP method developed in this study. In contrast, it is easy to determine suitable ranges or bounds for fault slip solutions, which are compatible with a particular earthquake rupture.

4.2. Comparisons Between the Yushu Earthquake Model of This Study and Other Results

4.2.1. The Three-Step MAP Inversion Model and the Field Investigation Results

[61] We predicted surface displacements on the fault based on our preferred model and compare it with the field measurements conducted by *Chen et al*. [2010] and *Sun et al*. [2010] (Figure 7c). The three-segment model and its predicted ground offsets are in good agreement with the field observations of the 67 km length surface rupture and fissures discovered at several places. All of the 11 horizontal displacement measurements [*Chen et al*., 2010] are comparable to the model prediction except for two points with larger model values, and the peak slip from the three-step MAP inversion model (or the "MAP model" for simplicity) is shifted ~8 km to the southeast of the largest offset observed in the field. This is due to the loss of InSAR coherence close to the fault, where the maximum slip of 2.1 m was observed in the field. It is interesting to see that the maximum slip predicted at the surface from our model and the corresponding measurements from the field investigations show comparable values at the same place.

4.2.2. The MAP Model and the FBI Model

[62] We implement two Monte Carlo approaches to invert for coseismic rupture models of the Yushu earthquake using

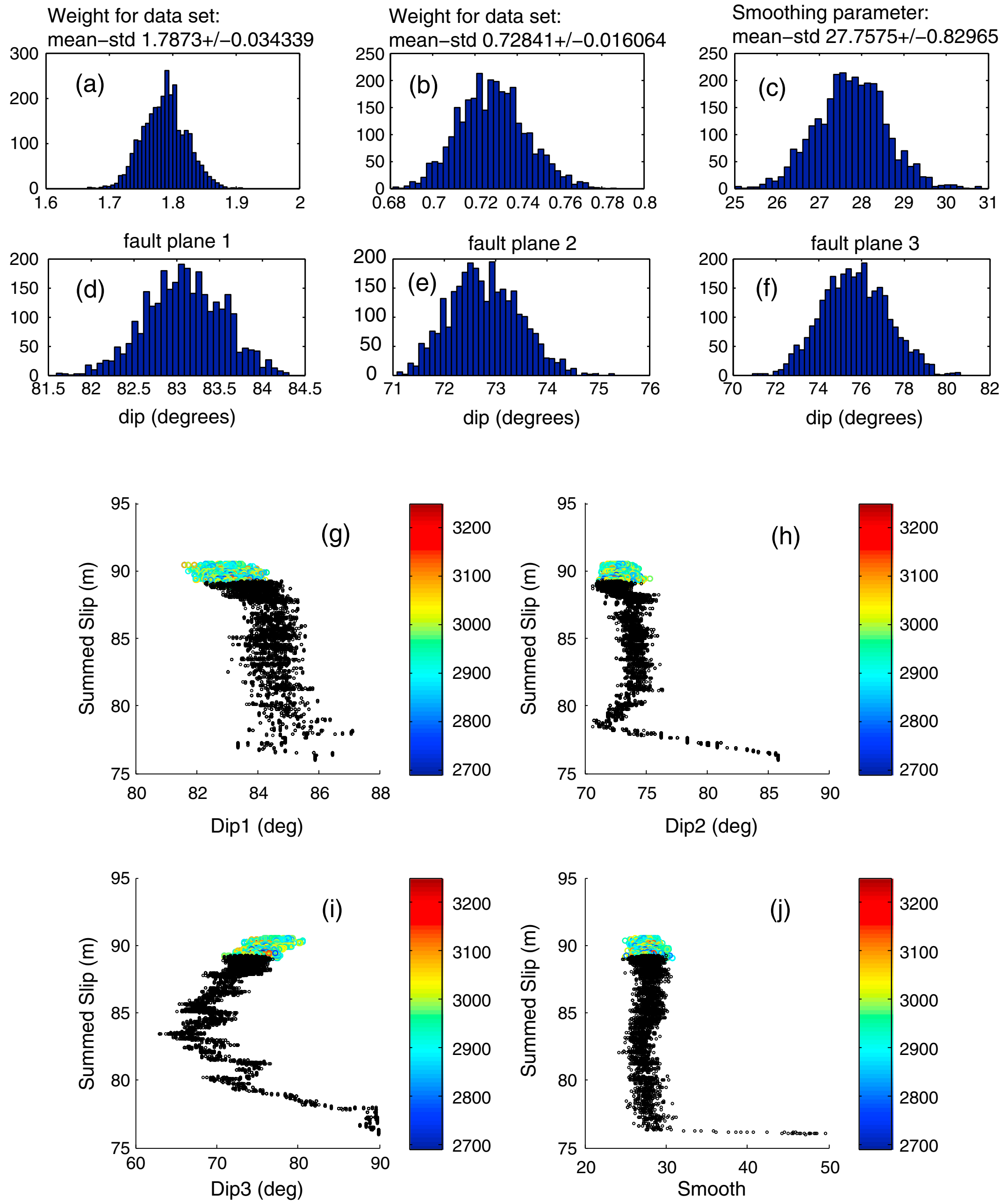

Figure 13. The 1-D and 2-D parameter distributions from the FBI method using the three-segment fault model. The models are sampled in a multidimensional parameter space, discarding those burn-in samples that are dependent on the initial model guesses. (a–f) Histograms of the inverted parameters. (g–j) The 2-D distributions of the summed slip versus the fault dips and smoothing factor excluding the burn-in samples (black points). The color bars represent the posterior probabilities of the inversion results.

InSAR data, namely, the FBI method as an ensemble inference process and the three-step MAP inversion as an optimization process. The differences between the two inversion results can be examined by comparing the slip-distribution models in Figures 6a and 7c. We used all of the three data sets with their full covariance models for the three-step MAP inversion, while the inversion is difficult to converge when using the same data sets and covariance models in the FBI method due to the complexity of the parameter space in this case. However, we find the basic features of the two slip-distribution models are very consistent (Figures 6a and 7c), such as the three strong slip areas on the three segments and the slip magnitudes. This indicates that the FBI model already provided an acceptable model for the Yushu earthquake, though only high-quality ascending pass InSAR data with diagonal covariance model are used in the inversion. The differences between the two inversion results are the dip angles of the three segments, which are 9°, 9°, and 3°, respectively, from the east to the west. Another difference is the maximum slip location on the slip solutions. The FBI

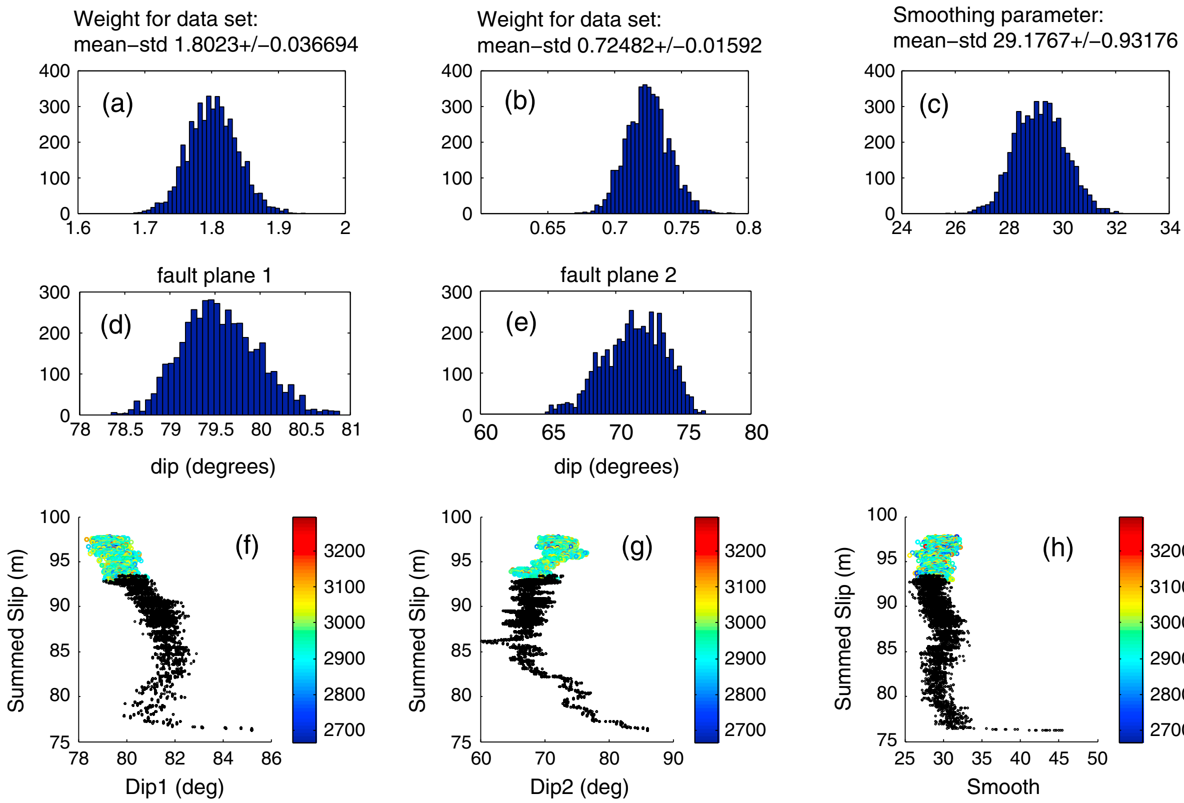

Figure 14. The 1-D and 2-D parameter distributions from the FBI method using the two-segment fault model. The models are sampled in a multidimensional parameter space, discarding those burn-in samples that are dependent on the initial model guesses. (a–e) Histograms of the inverted parameters. (f–h) The 2-D distributions of the summed slip versus the fault dips and smoothing factor excluding the burn-in samples (black points). The color bars represent the posterior probabilities of the inversion results.

model shows that the maximum slip occurred at a depth of 2.5 ~ 5.0 km though the slips at the east segment obviously ruptured the surface, while the maximum slip on the MAP model is located just at the surface.

[63] A more objective comparison between the FBI method and the MAP method is necessary using the same data sets for illustrating the advantages of the new method. We implement the first-step MAP inversion using the two ascending high-quality InSAR data sets, as used in the FBI inversion (Figure 6a). The results show that the three-segment models (Figure S13) are consistent with the FBI model, with all of the parameters inverted in their defined bounds. The fault geometry with a north dipping east segment (the Figure S13a model, with a little higher posterior PDF values than the Figure S13b model) is more consistent with the MAP inversion result in Figure 7c, though the dip angle on the middle segment has a 7° difference with it. The interesting point is that the slip-distribution model in Figure S13a is also quite similar to the final MAP inversion result (Figure 7c) using all of the three data sets. This test confirms the robustness of the MAP method in slip-distribution inversions and a different view angle of observation for better constraining fault geometry.

[64] We argue that the final model in Figure 7c from the three-step MAP inversion is more reliable because a number of factors are considered in this inversion: (1) The MAP inversion with a global optimization algorithm (ASA) is used to find a model close to the "true" model in the first-step inversion, and the problem of the FBI method getting trapped in low posterior PDF regions is avoided. (2) The noisy descending track data play a vital role in resolving fault dips. (3) The details of the MAP inversion method, such as the full covariance model, the new objective smoothing scheme, and the three-step process, make the final slip solution more clearly distributed in comparison with the FBI results. (4) The three-step MAP inversion works sequentially on the geodetic data, with the first-step MAP inversion guaranteeing the global optimization of the posterior PDF, while the second and third steps further refine the model.

4.2.3. The MAP Model and Models From Other Studies

[65] *Tobita et al.* [2011] used one pair of ALOS PALSAR data in ascending pass and a wide swath interferogram in descending pass to invert for the slip distribution of the Yushu earthquake. Their model shows that the maximum surface-slip of 1.66 m is located at WNW of Yushu. It is comparable to the maximum slip of 1.38 m in our model; however, the maximum slip of 2.6 m occurred at the lower part of the middle section of their model, which is only ~1.0 m maximum in our model here. The large difference of the slip magnitudes may originate from the lack of the high signal-to-noise ratio ASAR data on track 498 in their study. This interferogram plays a vital role in constraining the fault slip on the middle segment. *Tobita et al.* [2011] assumed only a vertical-segmented fault geometry in the inversion. Another study, which used similar data sets as ours and adopted the same inversion methods as in the work of *Wright et al.*

[1999] and *Funning et al*. [2005], finds that the middle segment dips 70° to the southwest and the other two segments are near vertical in their three-segment configuration [*Li et al*., 2011]. The dip angle differences are ~0.3°, 11.9°, and 10.6°, respectively, with our MAP model from the east segment to the west segment. The slip distribution of the model is similar to our preferred model in Figure 7c, with three large-slip areas along the fault. However, the slip magnitudes have some differences, especially on the middle segment, where our model shows that the slip on it is obviously smaller than the main rupture slip of the east segment, whereas the Li *et al*. model shows that the east and middle segments have similar slip magnitudes. In addition, though the east segment shows ~90.0° dip angle in both models, the maximum slip of 1.38 m of our model is at the surface, while it is ~1.5 m at a depth of 4 km in their model. It is hard to determine the reasons of the differences between our model and their model because errors in the InSAR data and/or the different inversion procedures all can lead to the model differences; however, we find that the basic features are the same in these two models.

[66] The benefits obtained from our new method relative to conventional methods come from two aspects. One aspect is the advantages inherited from the FBI and MBI methods, such as objective smoothing and data weights, and a unified solution for both fault geometry and slip solution without uniform slip assumptions. Another aspect is the advantage of a fast global optimization for posterior PDF of slip solution, so that a convergent and physically plausible model can always be obtained in short time. In addition, the earthquake rupture model is sequentially refined in the three steps of the MAP inversion, and it overcomes some well-known inversion shortcomings, such as the trade-off effects between parameters, the risk of being trapped in low posterior PDF regions, and the difficulty for optimization/sampling in discontinuous parameter space.

4.3. The FBI Method Convergence Process

[67] In Figure 7, we provided the evolving values of the seven nonlinear parameters in the MAP inversion. It is also important to assess the FBI method convergence process in Figure 6, so that the two classes of Monte Carlo inversion methods can be directly compared. We plot the histograms of the inverted parameters of the sampled models in a multidimensional parameter space, discarding those burn-in samples that are dependent on the initial model guesses (Figures 13 and 14 for the three-segment and two-segment cases, respectively). We see that all of the parameters lie within a narrow range with one peak value. We also plot the 2-D distributions of the summed slip versus the fault dips and smoothing factor to check for the trade-off effects between them excluding the burn-in samples (black points in Figures 13 and 14). We find that there is slight correlation between the slip and the fault dips/smoothing factor within a narrow parameter range. Both the two-segment and the three-segment models show near-equal fitting to the data in the FBI method.

[68] As opposed to the FBI method, which intends to search for a group of models by posterior PDF sampling, the MAP inversion aims at finding one stable model which maximizes the posterior PDF of slip solutions. It is clear from Figure 8b that the nonlinear parameters get stabilized quickly after ~600 model generation, while the FBI method generated a number of models in the burn-in stage and discarded them from the inversion, especially when the initial model is far from the "true" model. If the initial model is as close as possible to the "true" model, the efficiency of the FBI method and the MBI method will be greatly improved. This actually is one of the aims of the first step of the MAP inversion using the ASA, following which the second and the third steps of the MAP inversion start from the globally optimized model. Since the first step of the MAP inversion is independent of the other two steps of the MAP inversion, it is possible to replace the last two steps with the FBI method and gain the advantages of the Bayesian inversion as well.

5. Conclusions

[69] We developed a three-step MAP inversion method for coseismic slip inversion using geodetic data obtained from multiple geodetic data sets, such as GPS and InSAR. The method is based on the FBI and MBI methods and aims at maximizing the posterior PDF of elastic deformation solutions of an earthquake rupture. A highly efficient global optimization algorithm, the ASA algorithm, is used to search for the maximum posterior PDF in the first step, which brings the model very close to the "true" solution and guarantees the global optimization of the posterior PDF. In the first step, we adopt the posterior PDF of the MBI algorithm as the objective function, in which the nonlinear parameters are determined by the global optimization process, and the slip parameters are initially inverted for using the least squares method without positivity constraints, and then bounded to within physically reasonable ranges by a slip-replacement operation. Both the ASA algorithm and the posterior PDF of the MBI method guarantee that the inversion jumps over local maximum regions in the high-dimensional parameter space quickly and converges to a physically reasonable solution. The second and third step inversions use the MCI algorithm for the optimization of the posterior PDF of the slip solutions, with positivity constraints (slip bounds) applied. In these two steps, we adopt the posterior PDF of the FBI method as the objective function for the optimization. The second step inversion approaches the "true" solution further with all parameters obtained from step one as the initial solution. Finally, slip artifacts are further eliminated from slip models in the third step of the MAP inversion with positivity constraints applied on slip parameters and fault geometry parameters fixed. The new method has the capabilities to overcome two difficulties in the FBI and MBI methods, which provide complete probability formulations for geodetic data inversions, but may be trapped in low posterior PDF regions and are difficult to converge in short time.

[70] We used the method for the InSAR data inversion of a large strike-slip earthquake, the 14 April 2010 M_w 6.9 Yushu (Qinghai, China) earthquake. From the three-step MAP inversion result using both ascending and descending track InSAR data, we conclude that (1) the Yushu earthquake is a nearly pure left-lateral strike-slip event with the rupture extending ~67 km. (2) The fault is composed of three segments. The eastern segment bears the main rupture reaching the surface and in proximity to the greatest earthquake damage area in Yushu County. The middle segment has a smaller slip peak at 5 ~ 10 km depth and is completely blind. The

western rupture segment is offset to the south across the 4.5 km wide Longbao Lake pull-apart basin. (3) The maximum slip is ~1.38 m appearing on the eastern segment at the surface and most of the slip occurred within 15 km depth. (4) The total seismic moment released is estimated as 2.32e+19 Nm, which is consistent with the USGS seismic estimate of 2.50e + 19 Nm.

[71] **Acknowledgments.** We thank ESA (through Dragon Project 5305) and UNAVCO Supersite for providing ASAR data and Sentinel Asia for providing PALSAR data used in this study. We thank Gareth Funning and an anonymous reviewer for their critical reviews, which greatly improved the manuscript, the Associate Editor for useful comments, and the Editor Assistant, Kristen Taylor, for great help in processing the manuscript. Copyright of the ASAR data and PALSAR data belongs to ESA and JAXA, respectively. RB acknowledges support from NSF grant EAR 1014880. ZK and JS acknowledge supports from NSFC grant 41090294 and IGCEA grant JB-11-06.

References

Agostini, G. D. (2003), Bayesian inference in processing experimental data principles and basic applications, *Rep. Prog. Phys.*, *66*, 1383–1420, doi:10.1088/0034-4885/66/9/201.

Akaike, H. (1980), *Likelihood and the Bayes Procedure in Bayesian Statistics*, pp. 143–166, University Press, Valencia, Spain.

Árnadóttir, T., and P. Segall (1994), The 1989 Loma Prieta earthquake imaged from inversion of geodetic data, *J. Geophys. Res.*, *99*(B11), 21,835–21,855.

Bro, R., and S. D. Jong (1997), A fast non-negativity-constrained least squares algorithm, *J. Chemometr.*, *11*, 392–401.

Bürgmann, R., M. E. Ayhan, E. J. Fielding, T. J. Wright, S. McClusky, B. Aktug, C. Demir, O. Lenk, and A. Türkezer (2002), Deformation during the 12 November 1999 Düzce, Turkey earthquake, from GPS and InSAR data, *Bull. Seismol. Soc. Am.*, *92*(1), 161–171, doi:10.1785/0120000834.

Chen, L. C., H. Wang, Y. K. Ran, X. Z. Sun, G. W. Su, J. Wang, X. B. Tan, Z. M. Li, and X. Q. Zhang (2010), Surface rupture of Yushu (Qinghai) M_s 7.1 earthquake and strong historical earthquakes, *Chin. Sci. Bull.*, *55*(13), 1200–1205.

Farr, T. G., et al. (2007), The shuttle radar topography mission, *Rev. Geophys.*, *45*, 1–33, doi:10.1029/2005RG000183.

Fialko, Y. (2004), Probing the mechanical properties of seismically active crust with space geodesy: Study of the coseismic deformation due to the 1992 *M*(*w*)7.3 Landers (Southern California) earthquake, *J. Geophys. Res.*, *109*, B03307, doi:10.1029/2003JB002756.

Fukahata, Y., and T. J. Wright (2008), A nonlinear geodetic data inversion using ABIC for slip distribution on a fault with an unknown dip angle, *Geophys. J. Int.*, *173*(2), 353–364.

Fukuda, J., and K. Johnson (2008), A fully Bayesian inversion for spatial distribution of fault slip with objective smoothing, *Bull. Seismol. Soc. Am.*, *98*(3), 1128–1146, doi:10.1785/0120070194.

Fukuda, J., and K. M. Johnson (2010), Mixed linear–nonlinear inversion of crustal deformation data: Bayesian inference of model, weighting and regularization parameters, *Geophys. J. Int.*, *181*(3), 1441–1458, doi:10.1111/j.1365-246X.2010.04564.x.

Funning, G. J., B. Parsons, T. J. Wright, J. A. Jackson, and E. J. Fielding (2005), Surface displacements and source parameters of the 2003 Bam (Iran) earthquake from Envisat advanced synthetic aperture radar imagery, *J. Geophys. Res.*, *110*, B09406, doi:10.1029/2004jb003338.

Gelman, A., G. O. Roberts, and W. R. Gilks (1995), *Efficient Metropolis Jumping Rules*, Oxford Univ. Press, Oxford, U. K.

Ingber, L. (1993), Simulated annealing: Practice versus theory, *J. Math. Comput. Modell.*, *18*(11), 29–57.

Jonsson, S., H. Zebker, P. Segall, and F. Amelung (2002), Fault slip distribution of the 1999 M_w 7.1 Hector Mine, California, earthquake, estimated from satellite radar and GPS measurements, *Bull. Seismol. Soc. Am.*, *92*(4), 1377–1389.

Li, Z., J. R. Elliott, W. Feng, J. A. Jackson, B. E. Parsons, and R. J. Walters (2011), The 2010 M_w 6.8 Yushu (Qinghai, China) earthquake: Constraints provided by InSAR and body wave seismology, *J. Geophys. Res.*, *116*, B10302, doi:10.1029/2011jb008358.

Miller, M. A., M. L. Amon, and P. W. Reinhardt (2000), Should one adjust the maximum step size in a Metropolis Monte Carlo simulation?, *Chem. Phys. Lett.*, *331*, 278–284.

Minson, S. (2010), A Bayesian approach to earthquake source studies, PhD thesis, Calif. Inst. of Technol., Pasadena, Calif.

Ni, S., W. Wang, and L. Li (2010), The April 14th, 2010 Yushu earthquake, a devastating earthquake with foreshocks, *Sci. China Earth Sci.*, *53*, 791–793, doi:10.1007/s11430-010-0083-2.

Okada, Y. (1992), Internal deformation due to shear and tensile faults in a half-space, *Bull. Seismol. Soc. Am.*, *82*(2), 1018–1040.

Rosen, P. A., S. Henley, M. Simons, and G. Peltzer (2004), Updated repeat orbit interferometry package released, *Eos Trans. AGU*, *85*(5), 47.

Sambridge, M., and K. Mosegaard (2002), Monte Carlo methods in geophysical inverse problems, *Rev. Geophys.*, *40*(3), 1009, doi:10.1029/2000RG000089.

Sandwell, D., D. Myer, R. Mellors, M. Shimada, B. Brooks, and J. Foster (2008), Accuracy and resolution of ALOS Interferometry: Vector deformation maps of the Father's Day intrusion at Kilauea, *IEEE Trans. Geosci. Remote Sens.*, *46*(11), 3524–3534.

Shen, Z., J. Sun, P. Zhang, Y. Wan, M. Wang, R. Burgmann, Y. Zeng, W. Gan, H. Liao, and Q. Wang (2009), Slip maxima at fault junctions and rupturing of barriers during the 2008 Wenchuan earthquake, *Nat. Geosci.*, *2*(10), 718–724, doi:10.1038/ngeo636.

Sun, J., Z. Shen, X. Xu, and R. Bürgmann (2008), Synthetic normal faulting of the 9 January 2008 Nima (Tibet) earthquake from conventional and along-track SAR interferometry, *Geophys. Res. Lett.*, *35*, L22308, doi:10.1029/2008GL035691.

Sun, J., K. M. Johnson, Z. Cao, Z. Shen, R. Bürgmann, and X. Xu (2011), Mechanical constraints on inversion of coseismic geodetic data for fault slip and geometry: Example from InSAR observation of the 6 October 2008 M_w 6.3 Dangxiong-Yangyi (Tibet) earthquake, *J. Geophys. Res.*, *116*, B01406, doi:10.1029/2010JB007849.

Sun, X., X. Xu, L. Chen, X. Tan, G. Su, J. Wang, Z. Li, and X. Zhang (2010), Characteristics of surface rupture of the M_s 7.1 Yushu, Qinghai province earthquake at two representative places, *Seismolog. and Geology*, *32*(2), 338–344.

Taylor, M., and A. Yin (2009), Active structures of the Himalayan-Tibetan orogen and their relationships to earthquake distribution, contemporary strain field, and Cenozoic volcanism, *Geosphere*, *5*(3), 199–214, doi:10.1130/ges00217.1.

Tobita, M., T. Nishimura, T. Kobayashi, K. X. Hao, and Y. Shindo (2011), Estimation of coseismic deformation and a fault model of the 2010 Yushu earthquake using PALSAR interferometry data, *Earth Planet. Sci. Lett.*, *307*(3–4), 430–438, doi:10.1016/j.epsl.2011.05.017.

Tong, X., D. T. Sandwell, and Y. Fialko (2010), Coseismic slip model of the 2008 Wenchuan earthquake derived from joint inversion of interferometric synthetic aperture radar, GPS, and field data, *J. Geophys. Res.*, *115*, B04314, doi:10.1029/2009JB006625.

Wang, R., F. Martin, and F. Roth (2003), Computation of deformation induced by earthquakes in a multi-layered elastic crust—FORTRAN programs EDGRN/EDCMP, *Comput. Geosci.*, *29*, 195–207.

Wright, T., B. Parsons, J. Jackson, M. Haynes, E. Fielding, P. England, and P. J. Clarke (1999), Source parameters of the 1 October 1995 Dinar (Turkey) earthquake from SAR interferometry and seismic body wave modelling, *Earth Planet. Sci. Lett.*, *172*, 23–37.

Yabuki, T., and M. Matsu'ura (1992), Geodetic data inversion using a Bayesian information criterion for spatial distribution of fault slip, *Geophys. J. Int.*, *109*(2), 363–375.

Zebker, H. A., P. A. Rosen, and S. Hensley (1997), Atmospheric effects in interferometric synthetic aperture radar surface deformation and topographic maps, *J. Geophys. Res.*, *102*, 7547–7563.